Imaging of acoustically coupled oscillations due to flow past a shallow cavity: effect of cavity length scale

P. Oshkai[a], M. Geveci[a], D. Rockwell[a],*, M. Pollack[b]

[a]*354 Packard Laboratory, Department of Mechanical Engineering and Mechanics, Lehigh University, 19 Memorial Drive West, Bethlehem, PA 18015-3085, USA*
[b]*Lockheed-Martin, P.O. Box 1072, Schenectady, NY 12301-1072, USA*

Abstract

Flow–acoustic interactions due to fully turbulent inflow past a shallow axisymmetric cavity mounted in a pipe, which give rise to flow tones, are investigated using a technique of high-image-density particle image velocimetry in conjunction with unsteady pressure measurements. This imaging leads to patterns of velocity, vorticity, streamline topology, and hydrodynamic contributions to the acoustic power integral. Global instantaneous images, as well as time-averaged images, are evaluated to provide insight into the flow physics during tone generation. Emphasis is on the manner in which the streamwise length scale of the cavity alters the major features of the flow structure. These image-based approaches allow identification of regions of the unsteady shear layer that contribute to the instantaneous hydrodynamic component of the acoustic power, which is necessary to maintain a flow tone. In addition, combined image analysis and pressure measurements allow categorization of the instantaneous flow patterns that are associated with types of time traces and spectra of the fluctuating pressure. In contrast to consideration based solely on pressure spectra, it is demonstrated that locked-on tones may actually exhibit intermittent, non-phase-locked images, apparently due to low damping of the acoustic resonator. Locked-on flow tones (without modulation or intermittency), locked-on flow tones with modulation, and non-locked-on oscillations with short-term, highly coherent fluctuations are defined and represented by selected cases. Depending on which of these regimes occur, the time-averaged Q (quality)-factor and the dimensionless peak pressure are substantially altered.
© 2004 Elsevier Ltd. All rights reserved.

1. Introduction

1.1. Overview of flow tones

The objectives of the current investigation are to determine the characteristics of locked-on flow tones, which involve coupling between: (a) the source due to an instability arising from flow past a shallow cavity, and (b) the long wavelength resonant acoustic modes of a pipe or duct connected to the cavity configuration.

The background information reflecting the state-of-the-art is summarized by Rockwell et al. (2003). Previous studies have provided considerable insight into the generation of flow tones. The variety of configurations addressed in these

---

*Corresponding author. Tel.: +1 610 758 4107; fax: +1 610 758 4041.
E-mail address: dor0@lehigh.edu (D. Rockwell).

studies include a jet through a system of orifice plates (Hourigan et al., 1990; Stoubos et al., 1999), a separated shear layer past a cavity resonator (DeMetz and Farabee, 1977; Elder, 1978; Elder et al., 1982; Nelson et al., 1981, 1983), and a separated layer past a resonant side branch in the form of a duct or pipe (Pollack, 1980; Bruggeman et al., 1989, 1991; Kriesels et al., 1995; Ziada and Bühlmann, 1992; Ziada and Shine, 1999). Rockwell (1983) and Blake (1986) describe the common elements associated with purely hydrodynamic oscillations. Howe (1975, 1980, 1998) addresses the issues arising in the presence of an acoustic resonator, where the predominant mechanism is influenced by the coexistence of hydrodynamic and acoustic fields.

The present investigation focuses on the case of an axisymmetric cavity bounded by pipes at either end. Rockwell et al. (2003) provided a detailed assessment of the pressure fluctuations associated with this configuration. The current study considers the effects of cavity geometry on the flow patterns inside the cavity. An overview of previous investigations that addressed physical aspects of this class of problems is given by Geveci et al. (2003), who also provide quantitative images for a single cavity geometry and one value of the cavity length. Previous related investigations include qualitative visualizations of flow patterns (Cremer and Ising, 1967; Bruggeman, 1987; Ziada, 1994; Kriesels et al., 1995; Hourigan et al., 1990; Nelson et al., 1981; Huang and Weaver, 1991) and pointwise measurements of flow characteristics (Elder, 1978; Elder et al., 1982; Schachenmann and Rockwell, 1980; Rockwell and Schachenmann, 1982a,b; Nelson et al., 1981; Zoccola, 2000).

The theoretical framework for the majority of these investigations is related to the integral for acoustic power generation, which was formulated by Howe (1975, 1980). The critical features of power generation according to this relationship are described by a variety of discrete models of the vortices in the shear layer (Howe, 1975; Nelson et al., 1983; Bruggeman et al., 1989) as well as distributed representations of vorticity (Hourigan et al., 1990; Kriesels et al., 1995; Hofmans, 1998). Radavich et al. (1999) numerically solved the compressible Navier–Stokes equations, thereby accounting for the interaction between the mean flow and the acoustic field.

1.2. Flow tone generation from a shallow cavity: unresolved issues

The current study focuses on the flow physics associated with acoustic tone generation due to flow past a shallow axisymmetric cavity. This configuration is distinguished from those described in the foregoing investigations in several respects, and a number of unclarified issues are apparent.

(a) *Composite structure of cavity shear layer and recirculation zone: effect on onset of flow tone.* The majority of the aforementioned investigations considered cavities in the form of a side branch or a Helmholtz resonator. For these configurations, the depth of the cavity is sufficiently large to allow an unobstructed development of the shear layer along the mouth of the cavity. Within the cavity, a recirculation cell exists. In contrast, for the case of a shallow cavity, little is known of the corresponding flow patterns. It is expected that the form and location of the recirculation cell within the cavity will be altered. Moreover, it is anticipated that, in limiting configurations, the shear layer will tend to attach to the cavity floor. These time-averaged changes of the flow along and within the cavity would be directly related to the unsteady development of the shear layer instability and the formation of vortices. As a result, the values of critical velocity and cavity length for onset of a flow tone would be modified relative to the case of a deep cavity.

(b) *Transformation from a fully turbulent inflow to organized oscillations past the cavity.* Previous investigations of tone generation due to flow past cavities have involved inflow boundary layers ranging from a highly accelerated laminar state to a fully turbulent state. For the latter case, little is understood of the transformation from a fully turbulent inflow to coherent oscillations of the shear layer past the cavity during generation of a flow tone. The manner in which this transformation occurs will influence the coherence of the hydrodynamic source, i.e., the unsteady shear layer, and thereby its effectiveness for excitation of the acoustic resonator. In particular, it is unknown whether the time-averaged turbulence characteristics of the unsteady shear layer, e.g., root-mean-square velocity fluctuations and Reynolds stresses, overshadow those of the inflow boundary layer during generation of a flow tone. If so, this would indicate that the inherent instability of the separated shear layer, along with effective forcing of the shear layer by the resonant acoustic field, allow rapid dominance of the unsteady shear layer above the background turbulence.

(c) *Formation of small- and large-scale vortical structures in cavity shear layer.* In accord with recent investigations of purely hydrodynamic oscillations of jet-edge (Lin and Rockwell, 2001a) and cavity (Lin and Rockwell, 2001b) configurations, it is expected that small-scale vortices will be formed from the leading edge of the cavity. The mechanisms by which these small-scale vortices develop into larger ones have not been addressed.

(d) *Effect of orientation of resonant acoustic field with respect to cavity shear layer.* The present study focuses on a flow configuration where the direction of acoustic waves is nominally aligned with the direction of flow. Hourigan et al. (1990) consider flow through a sequence of sharp-edged baffles (orifice plates) for the case where the acoustic waves were aligned with the centerline of the flow system. The configuration of interest in the present investigation is a single

axisymmetric cavity where a fully established turbulent boundary layer separates from the leading edge of the cavity. The direction of propagation of acoustic waves is aligned with the direction of flow, such that a resonant acoustic standing wave system is established between the open-ended entrance of the inlet pipe and the open end of the exhaust of the exit pipe. The acoustic wavelength is, for all cases considered, much longer than the cavity length, and a pressure node is located midway along the length of the cavity for all values of cavity length. This alignment of the acoustic waves with the throughflow has been investigated only in a limited sense, relative to a more frequently pursued case where the acoustic waves are orthogonal to the direction of the mean flow. The orientation of the acoustic waves is expected to influence the effectiveness of the conversion from the oscillating acoustic field to the unsteady velocity and vorticity fluctuations in the shear layer immediately downstream of the separation edge. Furthermore, the orientation of the acoustic field is central to the generation of acoustic power for all regions of the cavity shear layer, as will be described in Section 7. These features have received relatively little attention via quantitative imaging of instantaneous, wholefield patterns of the flow structure.

(e) *Instantaneous hydrodynamic contributions to acoustic power generation*. The effect of cavity geometry on global, instantaneous representations of the flow patterns associated with tone generation has not been investigated. Of particular interest are patterns of both the instantaneous vorticity and the curl of velocity with vorticity, which represents the hydrodynamic contribution to the acoustic power integral of Howe (1975, 1980, 1998). These types of instantaneous patterns are expected to show the locally large amplitudes of the hydrodynamic contribution due to small-scale vortices, large-scale vortices, and overall undulations of the unsteady shear layer. Of course, these instantaneous patterns determine the phase-averaged patterns. The sequence of instantaneous states is the direct route to tracing the physical origin of the hydrodynamic contribution to the acoustic power.

(f) *Categorization of locked-on and nonlocked-on oscillations: instantaneous flow patterns in relation to pressure spectra*. During the generation of flow tones, the flow patterns are assumed to be phase locked from cycle to cycle of the flow tone oscillation. This feature has been clearly established for the above-mentioned configurations. The present configuration of a turbulent flow past a long, shallow cavity bounded by pipes at either end may yield resonant acoustic amplitudes that are relatively small, and thereby deviations from a locked-on state of the hydrodynamic field. The consequence would be departure of the pressure signal from a periodic form to a modulated or intermittent form, and alteration of the time-averaged pressure spectra, in particular the amplitude and the Q (quality) factor of the predominant spectral peak. Examination of successive instantaneous images of the flow patterns would allow determination of the origin of modulated or intermittent states, which would be enhanced by proximity of the floor of a shallow cavity.

The aim of the present investigation is to clarify the foregoing issues using a technique of high-image-density particle image velocimetry in conjunction with pressure measurements.

2. Experimental system and techniques

The experimental system used in the current investigation provided quantitative flow visualization and simultaneous acoustic pressure measurements. The experimental system and detailed specification of inflow conditions are described in detail by Geveci et al. (2003) and Rockwell et al. (2003). The key features of the system are described in the following.

The air supply and conditioning system is isolated from the actual experimental facility by a ceramic wall and consists of an air compressor, compressed air plenum, and an air dryer–filter unit. The conditioned air is transmitted to the actual pipeline–cavity system through an arrangement of pressure valves and regulators as described by Rockwell et al. (2003). In order to ensure that all of the upstream flow generation conditioning and valve systems were acoustically isolated from the main test-section, a long rubber hose was employed to connect the exit of the upstream valve/ regulator arrangement to the inlet of the plenum of the test-section. This very effectively damped out all extraneous disturbances. Acquisition of detailed pressure spectra over a wide range of flow velocity showed no spurious spectral components.

2.1. Pipeline–cavity system

The inlet plenum of the pipeline–cavity system is constructed from Plexiglas, and houses a 2.5 in (63.5 mm) thick layer of honeycomb, which acts as a flow straightener. The inside of the plenum is lined with acoustic damping foam to minimize local acoustic resonances.

The exit of the plenum contains a contraction, which was designed in order to avoid localized separation in the pipe inlet. To ensure that the large changes in pressure gradient near the exit of the nozzle did not produce localized

perturbations that would propagate downstream and, furthermore, to generate a fully turbulent boundary layer, a trip ring was located immediately downstream of the exit of the plenum contraction. This ring was located a distance of 35 mm from the pipe inlet. It had a thickness of 1 mm, and was 4 mm long. Its geometry involved a series of adjacent triangular cuts along the leading edge of the ring, in order to hasten the generation of small-scale, three-dimensional vortices, which promote the transformation to a fully turbulent boundary layer at the inlet to the cavity.

Two versions of the pipeline–cavity arrangement were constructed. The first version of this system, shown in Fig. 1, consisted of two 2400 mm (8 ft) segments of 25.4 mm (1 in) I.D aluminum piping, located on the upstream and downstream sides of the Plexiglas cavity. The second version of the pipeline–cavity system employed the same inlet plenum and cavity; however, shorter inlet (upstream) and exhaust (downstream) pipe sections were employed. These sections were 305 mm (1 ft) long. Unless indicated otherwise, all measurements described herein were performed using the short pipe system.

Multiple pressure transducers were located along the inlet and exhaust pipes. For the purpose of the present investigation, the reference pressure was measured at a location of 127 mm upstream of the leading edge of the cavity.

2.2. Cavity subsystem

The schematic of the cavity subsystem is shown in Fig. 2. The cavity is formed by fitting a Plexiglas tube over two Plexiglas sleeves, connected to inlet and exhaust aluminum pipes, designated as pipes A and B in Fig. 2. The left end of the Plexiglas tube slides along the exterior of a smoothly machined exterior surface of the sleeve connected to the inlet pipe A. This sliding arrangement allows adjustment of the cavity length L with a high degree of accuracy and repeatability. This adjustment was achieved by employing a traverse mechanism, which translated the entire pipe B and the Plexiglas tube attached to it.

To allow effective application of particle image velocimetry (PIV), approximately one quadrant of the Plexiglas tube was machined away and replaced by a window made of 0.1 mm think sheet of acetate. This sheet was wrapped around the entire periphery of the interior of the Plexiglas tube. Installation of this thin window allowed recording of the particle images illuminated by the laser sheet.

2.3. Pressure measurements and acoustic modes

A detailed description of the pressure measurement technique is provided by Rockwell et al. (2003). The significant features of this process are described in the following.

Piezoelectric pressure transducers with nominal sensitivity of 1727 mV/psi and vibration compensation were employed for pressure measurement. The pressure transducer a, located in the aluminum pipe A, as indicated in Fig. 2, was employed for all pressure measurements in the present investigation. Furthermore, it provided the reference signal for all PIV measurements.

The amplified and filtered pressure signals were digitized using an analog-to-digital board with 12-bit resolution. The sampling rate and the number of acquired samples were adjusted to obtain the frequency resolution of $\Delta f = 0.5$ Hz and the Nyquist frequency of 2048 Hz, which is well above the maximum frequency component of interest for this research.

The direction of the acoustic waves was aligned with the axis of the asymmetry of the pipeline–cavity system. For all cases considered, the acoustic wavelength λ was much larger than the cavity length L, which means that no acoustic resonance modes could be generated within the cavity. Furthermore, this relatively large wavelength condition also means that radial acoustic modes could not be produced. Taken as a whole, the inlet pipe–cavity–outlet pipe system constituted, in an approximate sense, an open–open pipe whereby the entrance of the inlet pipe and the exhaust of the outlet pipe provided the open–open boundary conditions. The acoustic resonant modes indicated herein, specifically in Figs. 3a and b, represent the $n = 1, 3, 5 \ldots$ resonant modes. The design of the pipeline–cavity system shown in Figs. 1 and 2 ensured that the pressure node of the acoustic standing wave system was maintained at the center of the cavity when the cavity length L was varied. Furthermore, pressure measurements at crucial locations in the flow system, including the pipe region upstream of the cavity, as well as within the cavity, show that the peak amplitude of the acoustic velocity fluctuation u_{ac} was approximately two orders of magnitude smaller than the centerline velocity of the inflow. In essence, this means that measured velocity field V can be viewed as essentially hydrodynamic.

2.4. Imaging of flow patterns

A digital version of particle image velocimetry (DPIV) was used to obtain two-dimensional velocity fields over a cross-section of the unsteady cavity flow. The airflow was seeded with olive oil particles having a mean diameter of one
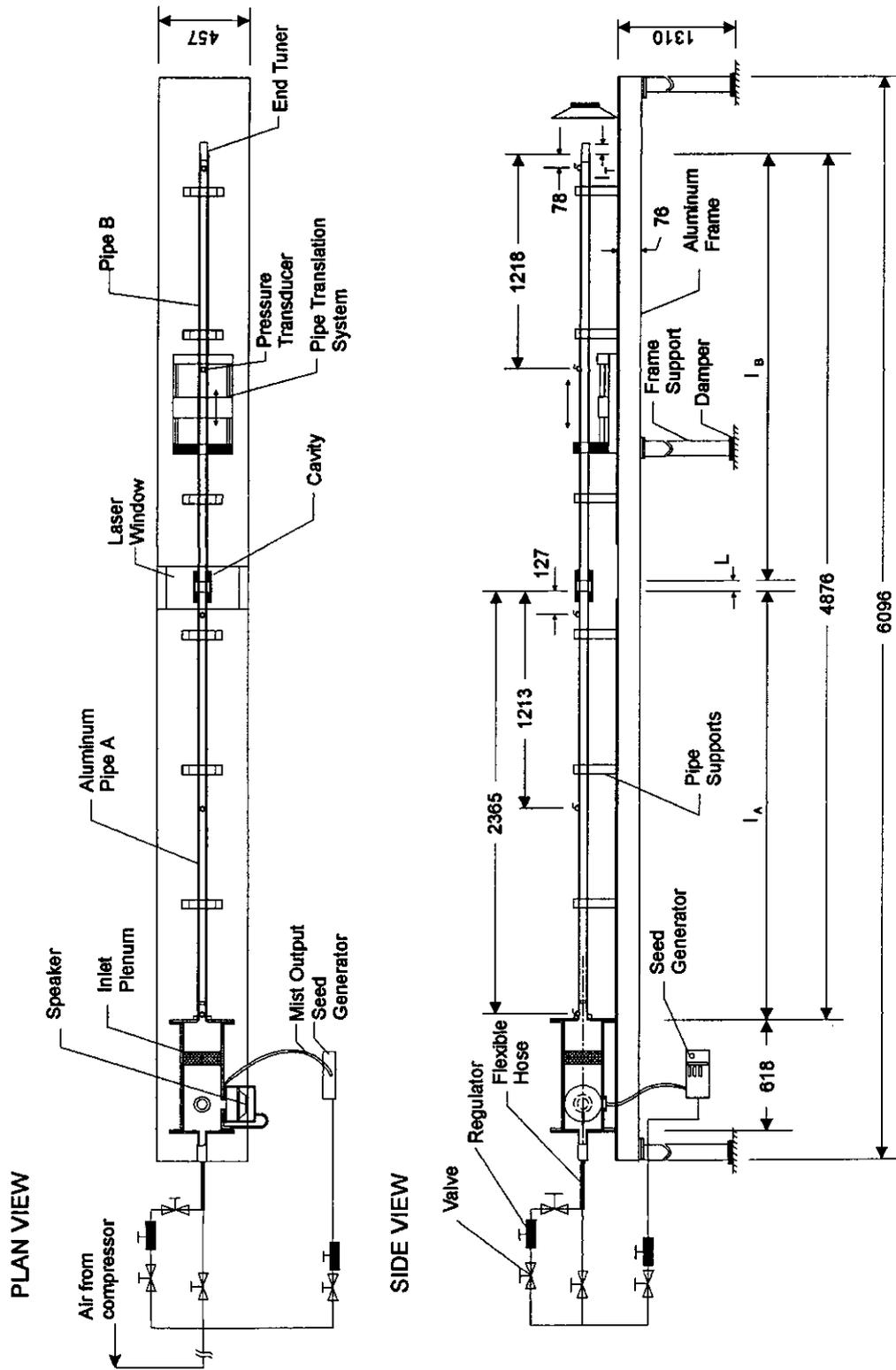
Fig. 1. Overview of pipeline–cavity system. [From Rockwell et al. (2003).]
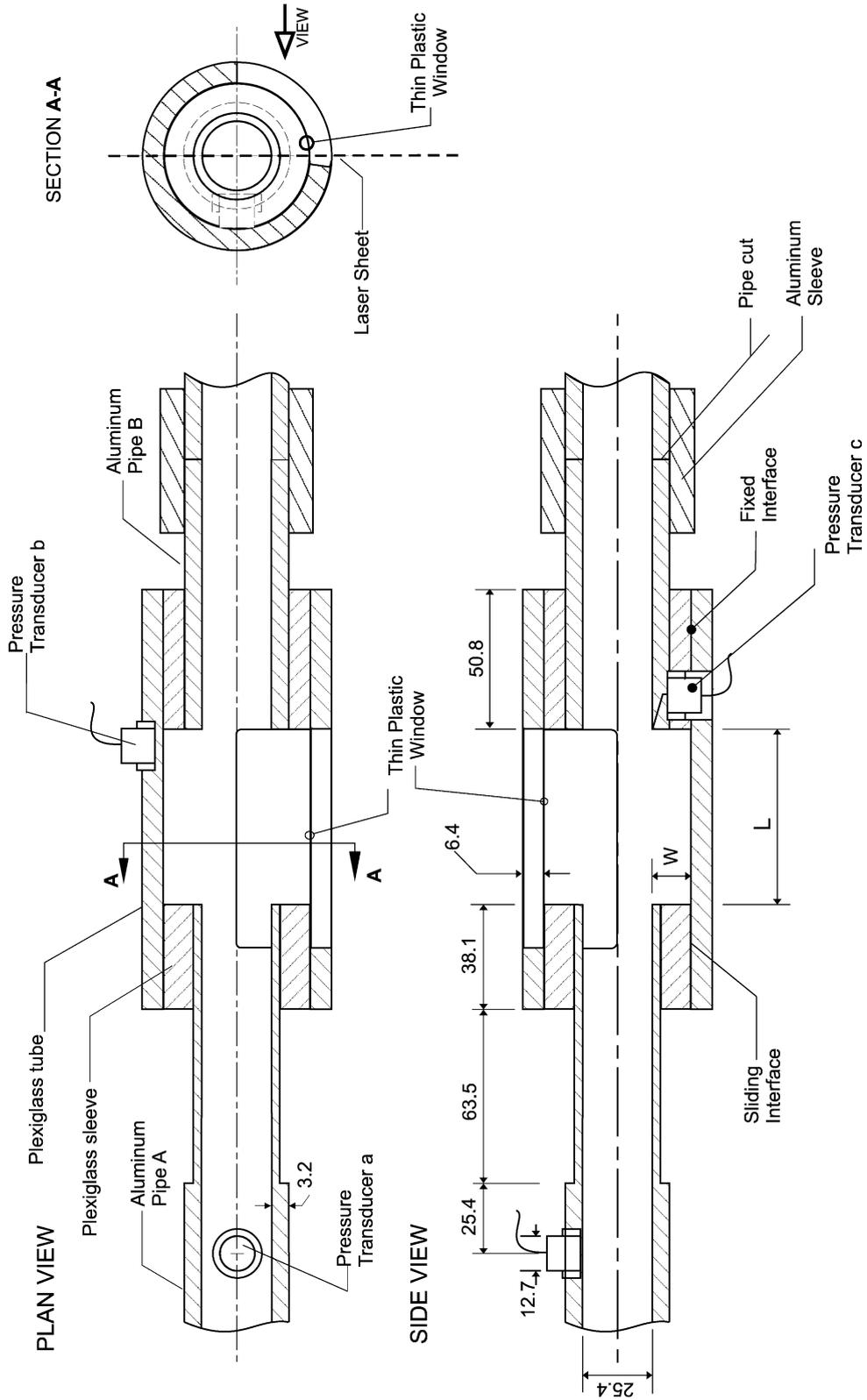
Fig. 2. Cavity subsystem employed for PIV imaging. [From Geveci et al. (2003).]

micron. The particles were generated by a six-jet atomizer. A laser sheet was generated from a dual, pulsed Nd:Yag laser system. This laser unit generates two successive pulses, with a spacing of 7 μs between pulses, which provides the optimum shift in the patterns of particle images.

A system consisting of a cylindrical and a spherical lens was used to transform the output laser beam into a laser sheet. The laser sheet had a thickness of approximately 1 mm and a width that exceeded the cavity length. The laser sheet was positioned at the centerline of the cavity. The precise alignment was achieved by placing the laser, along with the lens system, on a multi-degree-of-freedom positioning unit.

A digital charge-coupled device (CCD) camera was used to capture the images of particles for the two-frame cross-correlation version of DPIV. The CCD element has an active image area of a size of 9.07 mm × 9.16 mm consisting of 1008 × 1018 pixels. A lens with a focal length of 105 mm, combined with an extension tube, provided a magnification of
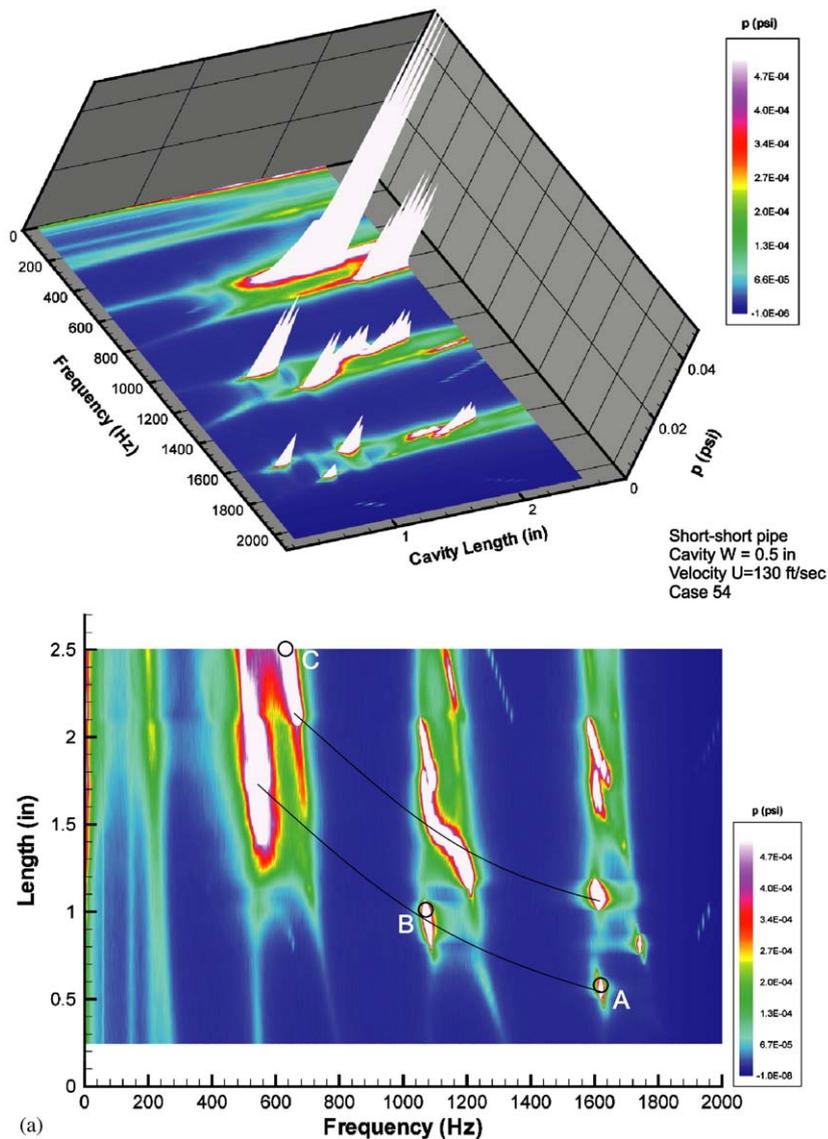
Fig. 3. (a) Isometric view (top image) and plan view (bottom image) of pressure amplitude as a function of frequency and cavity length. Lines shown on plan view represent fits through peak values of pressure amplitude. Plots are based on Oshkai et al. (2005) and correspond to (a) $W = 0.5$ in (12.7 mm), $U = 130$ ft/s (39.62 m/s); (b) $W = 0.25$ in (6.4 mm), $U = 118$ ft/s (35.97 m/s) for short pipes on either side of cavity.
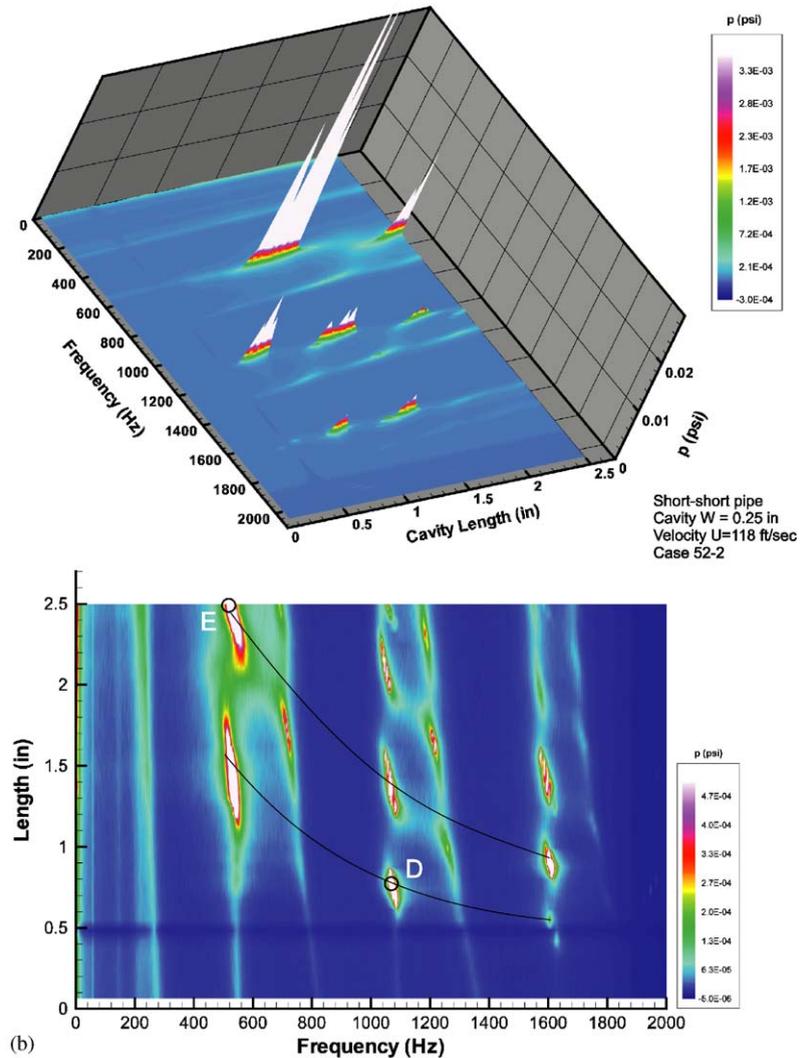
Fig. 3. (*Continued*)

1:7.3. The camera was used at its maximum framing rate of 30 frames/s, which provides 15 pairs of cross-correlated DPIV images per second.

A velocity field was obtained from each pair of Tagged Image File Format (TIFF) image files using a cross-correlation method involving two successive fast Fourier transforms. The total number of spurious vectors was only 2 percent of the total number of vectors. These spurious vectors were replaced by employing an interpolation routine. A Gaussian filter with an exponent of $p = 1.3$ was then implemented, as discussed by Landreth and Adrian (1989).

2.5. Time averaging of PIV images

As mentioned in the previous section, the PIV images of the velocity field inside the cavity were acquired at an interval of 1/15 s. Taking into account the relatively high nominal frequency of the shear layer oscillation, this spacing in time is suitable for obtaining random samples for calculation of averaged turbulence statistics.

The definitions of the time-averaged parameters are provided by Geveci et al. (2003). They are summarized below. A total of 128 images were acquired for each case considered in the present investigation. The total number of images is represented by N in the following definitions:

time-averaged horizontal component of velocity:

$$\langle u \rangle \overset{\Delta}{=} \frac{1}{N} \sum_{n=1}^{N} u_n(x, y); \tag{2.1}$$

time-averaged transverse component of velocity:

$$\langle v \rangle \overset{\Delta}{=} \frac{1}{N} \sum_{n=1}^{N} v_n(x, y); \tag{2.2}$$

time-averaged vorticity:

$$\langle \omega \rangle \overset{\Delta}{=} \frac{1}{N} \sum_{n=1}^{N} \omega_n(x, y); \tag{2.3}$$

root-mean-square of u component fluctuation:

$$u_{\text{rms}} \overset{\Delta}{=} \left\{ \frac{1}{N} \sum_{n=1}^{N} [u_n(x, y) - \langle u(x, y) \rangle]^2 \right\}^{1/2}; \tag{2.4}$$

root-mean-square of v component fluctuation:

$$v_{\text{rms}} \overset{\Delta}{=} \left\{ \frac{1}{N} \sum_{n=1}^{N} [v_n(x, y) - \langle v(x, y) \rangle]^2 \right\}^{1/2}; \tag{2.5}$$

averaged value of Reynolds stress correlation:

$$\langle u'v' \rangle \overset{\Delta}{=} \frac{1}{N} \sum_{n=1}^{N} [u_n(x, y) - \langle u(x, y) \rangle] [v_n(x, y) - \langle v(x, y) \rangle]. \tag{2.6}$$

3. Effect of cavity geometry (length and width) on locked-on flow patterns: selection of conditions for image acquisition

In order to determine the most appropriate conditions for imaging of locked-on flow tones as a function of cavity length L and depth W, extensive data on fluctuating pressure were assessed. Variations of cavity length L at fixed values of cavity depth W and flow velocity U were considered, whereby U was selected to be sufficiently high, such that flow tones would have a high probability of occurrence for a given cavity geometry. In addition to these experiments, variations of inflow velocity at fixed values of L and W were also addressed. These experiments are described by Rockwell et al. (2003) and Oshkai et al. (2005).

The focus of the present investigation is on the flow structure past very shallow cavities during generation of a flow tone. For this reason, two representative depths W of a shallow cavity were selected: $W/D = 0.5$ and 0.25, where D is the inflow pipe diameter. The value of $W/D = 0.25$, which corresponds to $W/\Theta = 20$, in which Θ is the inflow momentum thickness, is the smallest depth at which flow tones could be generated; $W/D = 0.125$, corresponding to $W/\Theta = 10$ did not yield flow tones.

A motivation for selection of representative values of cavity length L and depth W is centered on occurrence of basic hydrodynamic modes (stages) of the shear layer along the cavity. The traditional, simplistic view is that the first and second stages correspond to occurrence of one and two vortices in the shear layer along the cavity. In addition, it is hypothesized that another form of stage 1, which corresponds to deflection of the shear layer in absence of formation of a single vortex, may be attainable during generation of a flow tone. Based on extensive preliminary imaging of the flow structure, values of geometrical parameters and inflow velocity were selected to illustrate these basic stages of oscillation.

The three-dimensional views at the top of Figs. 3a and b show the pressure amplitude p on a plane of frequency f versus cavity length L. Plan views of these three-dimensional representations are shown in the bottom images of Figs. 3a and b. The solid black lines correspond to fits through peak values of pressure amplitude. For the present effort involving acquisition of flow images during a locked-on flow tone, the selected values of cavity length L are indicated by the open circular symbol.

Table 1
Definition of cases of cavity oscillation referred to in Figs. 3a and b

Case	W/D	L/D	fD/U	$f\theta/U$	$p/\frac{1}{2}\rho U^2$	$p/\rho Uc$	L/λ
A	0.5	0.595	1.032	0.0132	0.136	0.008	0.071
B	0.5	1.04	0.705	0.0090	0.170	0.010	0.084
C	0.5	2.5	0.391	0.0050	0.204	0.012	0.112
D	0.25	0.78	0.777	0.0099	0.120	0.006	0.063
E	0.25	2.5	0.431	0.0055	0.359	0.019	0.112

In Fig. 3a, cases A, B and C correspond, respectively, to: lateral deflections of the shear layer without formation of a large-scale vortex; formation of a single, large-scale vortex; and formation of two large-scale vortices along the path of the cavity. In Fig. 3b, cases D and E represent, respectively, lateral deflections of the shear layer in absence of large-scale vortex formation; and occurrence of two large-scale vortices along the cavity.

Table 1 shows dimensionless parameters for each of the cases A–E designated in Figs. 3a and b. Values of fL/U are typically employed to designate the hydrodynamic mode (stage) of the unstable shear layer along the cavity that locks onto the resonant acoustic mode to produce a flow tone. In absence of acoustic resonance effects, values of fL/U of the order of 0.5 represent the first hydrodynamic mode (stage), while values of the order of 1.0 correspond to the second hydrodynamic stage. The shear layer structure, corresponding to each of the values of fL/U in Table 1, are summarized in the preceding paragraph, and will be addressed subsequently when discussing the images of the flow structure. Concerning the values of fD/U, Rockwell et al. (2003) discuss the fact that values lying in the range $0.3 \lesssim fD/U \lesssim 0.6$ represent the band of frequencies over which large-scale vortices form downstream of an axisymmetric nozzle or pipe. As for values of $f\theta/U$, values lying in the range of $0.004 \lesssim f\theta/U \lesssim 0.034$ correspond to substantial values of amplification factor of the thin shear layer instability along the cavity. It is evident, from inspection of the values of fD/U and $f\theta/U$ for all of the cases given in Table 1, that an inherently unstable large-scale mode (based on D) and a small-scale mode (based on θ) occur.

In the following sections, the time-averaged and instantaneous flow patterns are characterized in detail for the representative geometries in Table 1.

4. Effect of cavity length on locked-on flow patterns: time-averaged and instantaneous images

Patterns of averaged streamfunction $\langle\psi\rangle$, i.e., averaged streamlines, root-mean-square values of the transverse velocity fluctuations, represented by v_{rms}, as well as the Reynolds stress correlation $\langle u'v'\rangle$ are given in Figs. 4a–c. In each figure, three representative values of cavity length were considered: $L/D = 0.595$, 1.04 and 2.5. The dimensionless cavity depth is maintained at $W/D = 0.5$. In order to obtain the averaged representations of the flow patterns of Figs. 4a–c, time averages were performed using the definitions of Section 2.5. A total of 128 instantaneous images were averaged to obtain each of the images presented in the figures. In other words, each image represents the consequence of 128 instantaneous states of the flow during generation of a flow tone.

4.1. Averaged patterns of flow structure

4.1.1. Patterns of averaged streamlines

Fig. 4a shows images of averaged streamlines, represented by $\langle\psi\rangle$, corresponding to dimensionless values of cavity length $L/D = 0.595$, 1.04 and 2.5 at a constant value of cavity depth $W/D = 0.5$. Irrespective of the cavity length, only a single recirculation cell exists within the cavity. That is, no counter rotating cells occur. Very small-scale cells may occur in the corners of the cavity, but were not detectable with the effective spatial resolution of the present imaging technique. Each large-scale, single recirculation cell is characterized by a limit cycle streamline near its center. This limit cycle is represented by the thick, white circular (or elliptical) closed contour. Spiral patterns of streamlines occur exterior and interior to this limit cycle.

An additional, remarkably consistent feature is that the center of each of the recirculation cells, i.e. the center of each limit cycle, occurs relatively close to the trailing (impingement) corner of the cavity. In fact, for increasing values of L/D, shown in the top, middle and bottom images, the center of the recirculation cell is situated approximately a distance
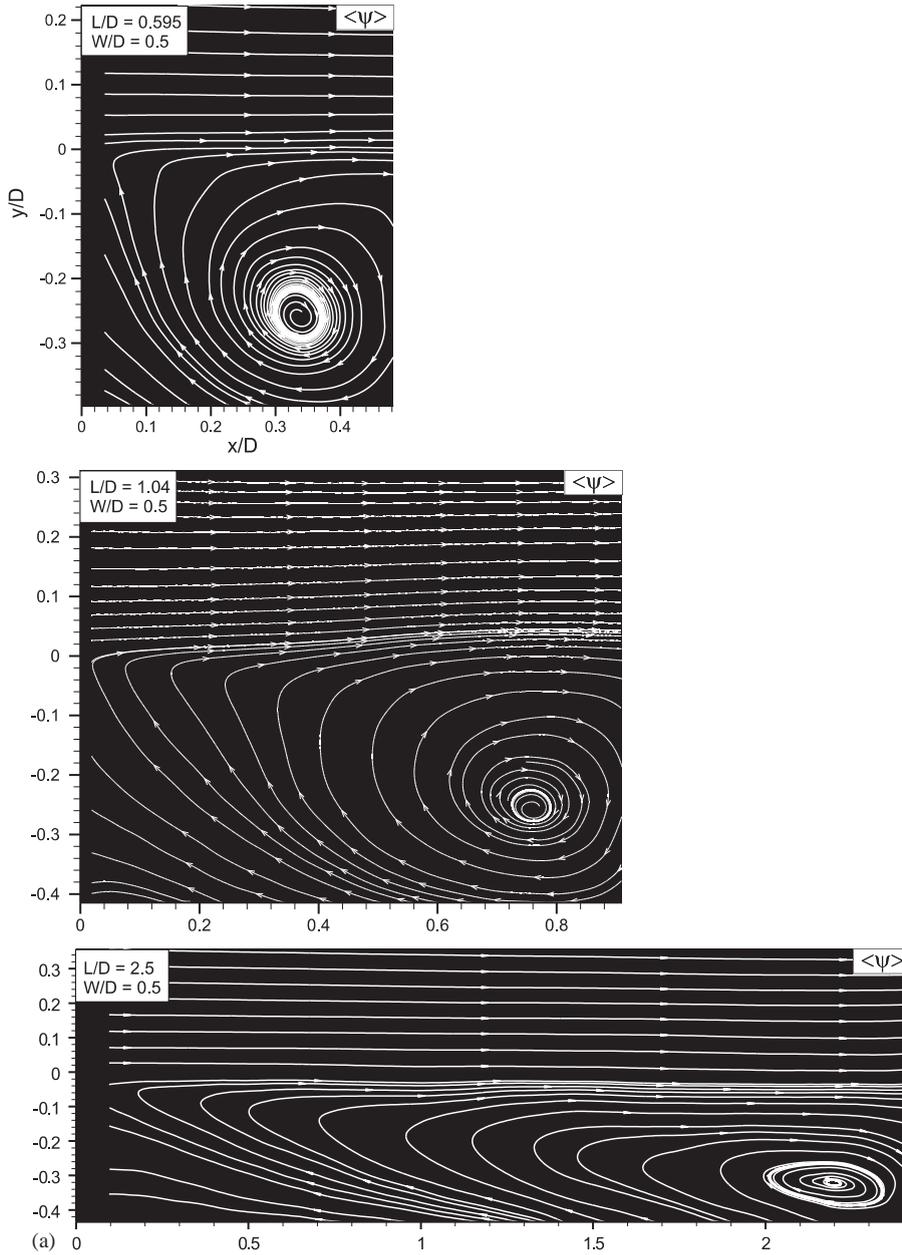
Fig. 4. (a) Comparison of time-averaged streamline patterns as a function of cavity length L for a constant value of cavity depth W, both of which are normalized by the diameter D of the inflow pipe. Inflow velocity is $U = 39.62$ m/s for top, middle and bottom images. These images (top to bottom) correspond to cases A, B and C in Fig. 3a. (b) Comparison of root-mean-square of the transverse velocity fluctuation v_{rms} as a function of cavity length L for a constant value of cavity depth W, both of which are normalized by the diameter D of the inflow pipe. Minimum contour levels are $(v_{rms})_{min} = 2.4$, 3.5, and 2.8 m/s, and incremental contour levels are $\Delta(v_{rms}) = 0.07$, 0.25, and 0.35 m/s for top, middle and bottom images. These images (top to bottom) correspond to cases A, B and C in Fig. 3a. (c) Comparison of time-averaged velocity correlation $\langle u'v' \rangle$ as a function of cavity length L for a constant value of cavity depth W, both of which are normalized by the diameter D of the inflow pipe. Minimum negative and positive contour levels are $(\langle u'v' \rangle)^-_{min} = -0.9$, -23.4, -18.0 m^2/s^2, and $(\langle u'v' \rangle)^+_{min} = 10.3$, 23.0, 21.0 m^2/s^2 for the top, middle and bottom images, and the corresponding incremental values are $\Delta(\langle u'v' \rangle) = 7.7$, 11.3, and 20.0 m^2/s^2. These images (top to bottom) correspond to cases A, B and C in Fig. 3a.
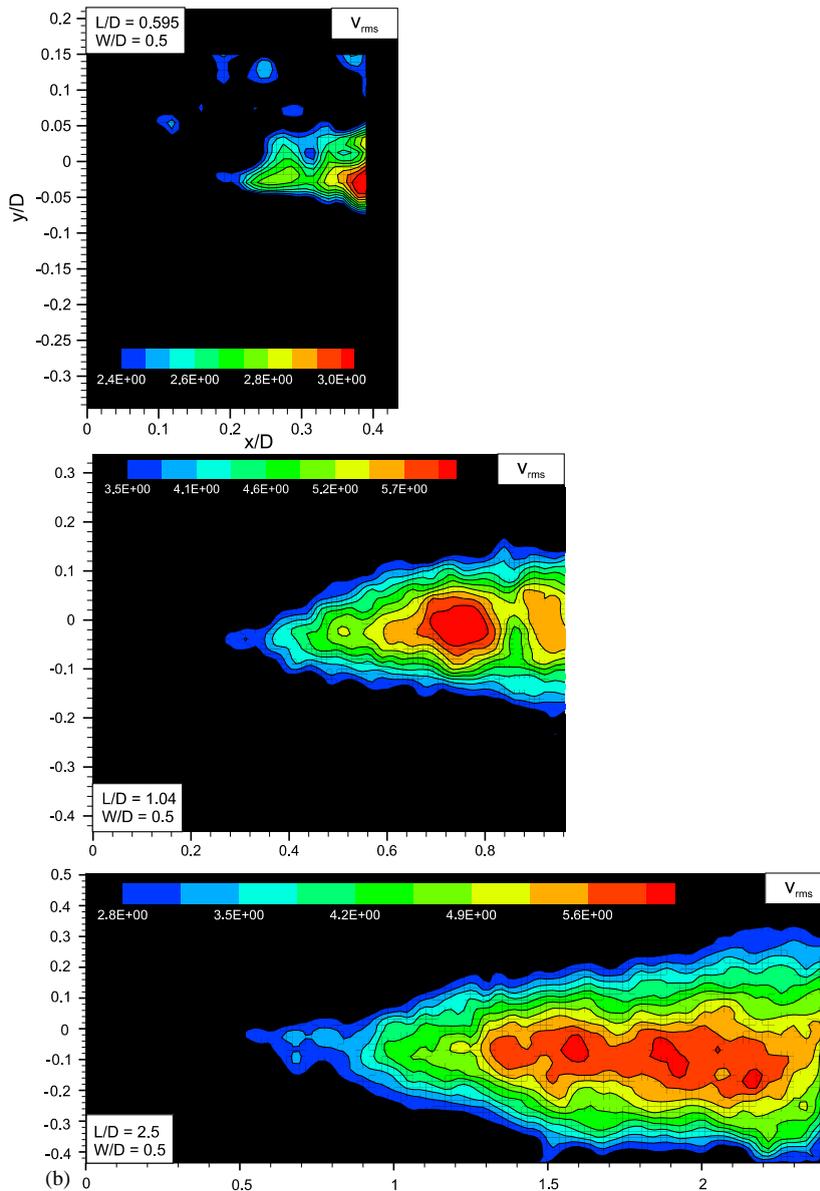
Fig. 4. (*Continued*)

of 0.15D, 0.21D and 0.30D upstream of the trailing (impingement) corner of the cavity. This location of the center of the recirculation cell apparently allows the proper amount of return flow to be swept downward along the vertical face of the trailing- (impingement-) corner of the cavity, then in the upstream direction along the floor of the cavity. Finally, the return flow is eventually drawn into the developing shear layer due to entrainment effects. In fact, the upward-oriented streamlines in the left region of each of the images of Fig. 4a are associated with the increase in volume (or mass) flow due to entrainment along the shear layer as it develops in the streamwise direction.

   A further consequence of the recirculation cell is that it maintains nearly horizontal streamlines at the impingement corner of the cavity, which is located at the elevation $y/D = 0$. That is, the separated shear layer along the mouth of the cavity, which impinges on the downstream corner of the cavity, is essentially in the horizontal direction immediately prior to impingement. In order for this condition to be maintained, the center of the recirculation cell must remain close to the trailing-corner of the cavity for all values of L/D.
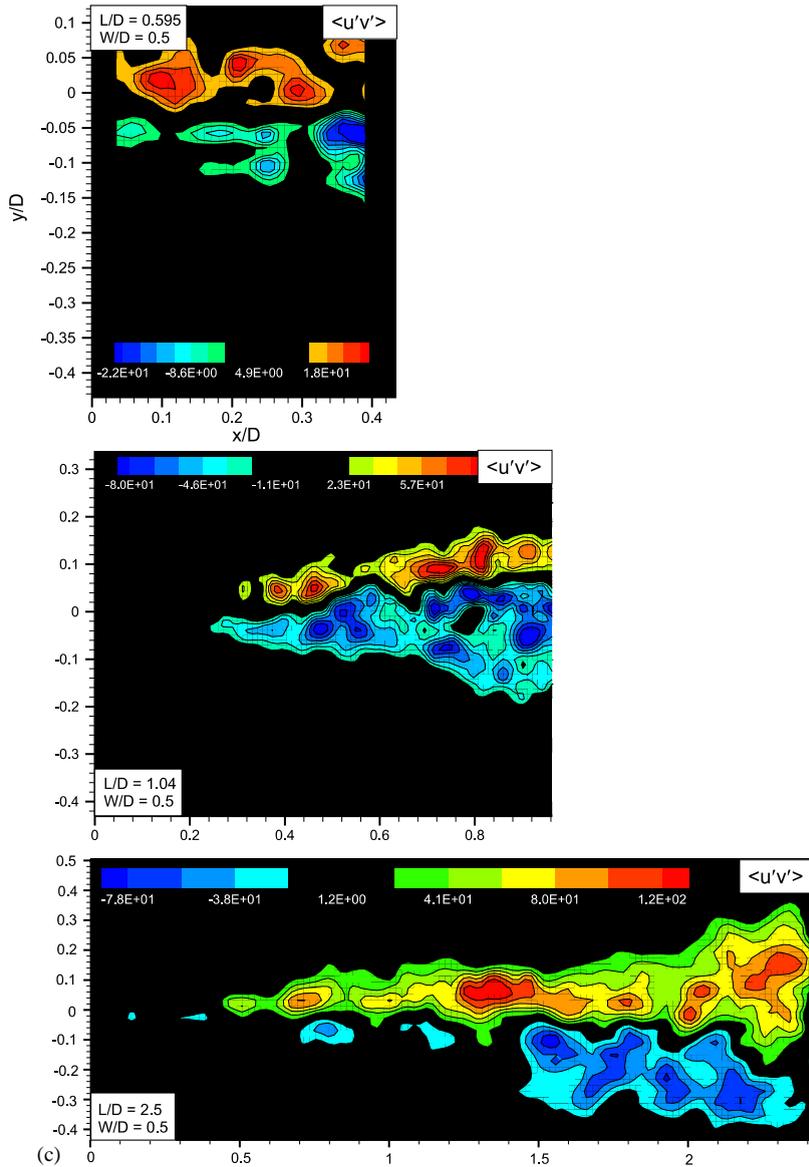
Fig. 4. (*Continued*)

4.1.2. Averaged magnitude of velocity fluctuations

Fig. 4b shows the root-mean-square distribution of the transverse velocity fluctuations, v_{rms}. The images indicate that significant levels of v_{rms} occur in the separated shear layer along the cavity, i.e. along the height $y/D = 0$, and are most prevalent at locations well downstream of the leading corner of the cavity. These fluctuations may be due to one or a combination of the following: (a) broadband turbulence; (b) organized undulations of the separating shear layer in absence of large-scale vortex formation; and (c) formation of large-scale vortical structures. Regarding category (a), the effects of broadband turbulence are expected to be most pronounced in the initial region of the shear layer at the leading corner of the cavity, where the inflow effects of the broadband turbulent boundary layer will be dominant, except for contributions from very small-scale vortices, which are present in that region. In this initial region, large-scale, organized undulations have not had an opportunity to develop. All of the images of Fig. 4b show significantly smaller levels of v_{rms} in this initial region of the shear layer development, which suggests that the contribution from category (a), due to broadband turbulence, is not predominant in the downstream region of the shear layer.

Concerning contributions from categories (b) and (c), associated, respectively, with organized undulations of the shear layer and vortex formation within the shear layer, corresponding instantaneous images are required in order to distinguish between these possibilities. In fact, instantaneous images of the flow structure, which are described below, do indeed show the existence of large-scale vortices that correspond to regions of large v_{rms} at $L/D = 1.04$ and 2.5 in Fig. 4b, whereas only transverse undulations of the shear layer, in absence of large-scale vortex formation, are distinguishable within the field of view of the images of v_{rms} at $L/D = 0.595$.

An important feature of the patterns of v_{rms}/U, shown in Fig. 4b, is their overall width, relative to the width W of the cavity. From the images of Fig. 4b, it is evident that the region of significant fluctuations in the shear layer occupies an increasing fraction of the cavity depth W as the cavity length L/D increases. In fact, for the extreme case of the pattern of v_{rms}/U shown in the bottom image of Fig. 4b, the width of the region of significant fluctuations extends over a major portion of the cavity depth. This observation emphasizes the distinctive nature of oscillations along a shallow cavity. Unlike a deeper cavity, where the fluctuating shear layer is located above a recirculation zone of relatively low-level fluctuation intensity, the fluctuating shear layer of the shallow cavity occupies the entire cavity depth and is intertwined with the recirculation zone.

4.1.3. Patterns of Reynolds stress correlation

Fig. 4c shows contours of constant Reynolds stress correlation $\langle u'v' \rangle$. A consistent feature of the patterns at all values of L/D is the occurrence of layers of positive and negative $\langle u'v' \rangle$ immediately adjacent to each other and extending over a substantial fraction of the cavity length. The interface between these positive and negative patterns is approximately centered at the elevation $y/D = 0$. As the cavity length L/D increases, the maximum values of the Reynolds stress $[\langle u'v' \rangle]_{max}/U^2$ show substantial increases.

For the case of broadband turbulence in the free-shear layer, or ill-defined large-scale vortical structures, it is expected that only a single layer of the Reynolds stress correlation $\langle u'v' \rangle$ would be present. It is known, however, that for a shear layer excited by an external source such as a loudspeaker, both positive and negative contours of the Reynolds stress correlation $\langle u'v' \rangle$ can occur in a free shear layer in absence of a bounding cavity. The interesting feature of the patterns of Fig. 4c is that positive and negative concentrations of $\langle u'v' \rangle$ are not interlaced with each other. Rather they appear in two distinct layers.

A further feature of the patterns of Reynolds stress is their overall width. For the longest cavity $L/D = 2.5$, substantial levels of Reynolds stress extend over a transverse distance larger than the cavity depth.

4.2. Instantaneous patterns of flow structure

4.2.1. Patterns of instantaneous vorticity and velocity

The time-averaged patterns described in the previous sections are, of course, a consequence of the instantaneous flow structure. Figs. 5a–c show patterns of instantaneous vorticity ω, total velocity V and vertical component of velocity v for the same values of cavity length L/D as for Figs. 4a–c. The images of instantaneous vorticity ω were selected from a large number of randomly acquired images; the attainment of maximum scale of the well-defined cluster(s) of vorticity was used as a selection criterion. For the images at the shortest cavity length, no such large-scale vortex appears, and therefore no criterion was applied.

The patterns of instantaneous vorticity shown in Fig. 5a indicate, first of all, the occurrence of large-scale vortical structures at the largest values of cavity length $L/D = 1.04$ and 2.5. The spatial locations at which these large-scale vortices appear are in accord with the range of x/D for which large values of v_{rms} occur in Fig. 4b. Furthermore, the locations of these large-scale vortices are in general accord with the regions of high Reynolds stress correlation $\langle u'v' \rangle$ in Fig. 4c.

In addition to the link between the patterns of large-scale vortices in Fig. 5a and the time-averaged patterns of Figs. 4a–c, each of the instantaneous patterns of Fig. 5a provides important insight into the characteristics of the shear layer that are associated with locked-on flow tones. The image that represents the shortest cavity length $L/D = 0.595$ does not show large-scale vortex formation. Rather, a substantial upward deflection of the shear layer is evident. Examination of other randomly acquired instantaneous images over various phases of the oscillation cycle verified the fact that this transverse deflection, in absence of formation of a significant large-scale vortical structure, is a key element of the flow pattern along a very short cavity during generation of a tone. If a flow system with similar geometry as that employed herein would involve substantially lower values of damping, i.e., substantially higher values of Q factor, then higher excitation levels may be attainable and, in this case, it is possible that vortex formation could occur for this shortest cavity length L/D. The intent of the present observation, however, is to emphasize that generation of a pronounced flow tone can occur at short cavity lengths in absence of large-scale vortex formation.

At a larger value of cavity length $L/D = 1.04$, the initial region of the shear layer is also deflected in the upward direction, in a fashion similar to that at $L/D = 0.595$. Further downstream, however, at location $x/D = 0.65$, formation of a large-scale vortical structure is evident. At a still further location downstream, the shear layer again shows an upward deflection.

For the largest value of cavity length $L/D = 2.5$, shown in Fig. 5a, two large-scale vortical structures occur. They are preceded by a nominally horizontal layer of vorticity. That is, substantial upward deflection of the vorticity layer prior to formation of large-scale vortex does not occur.
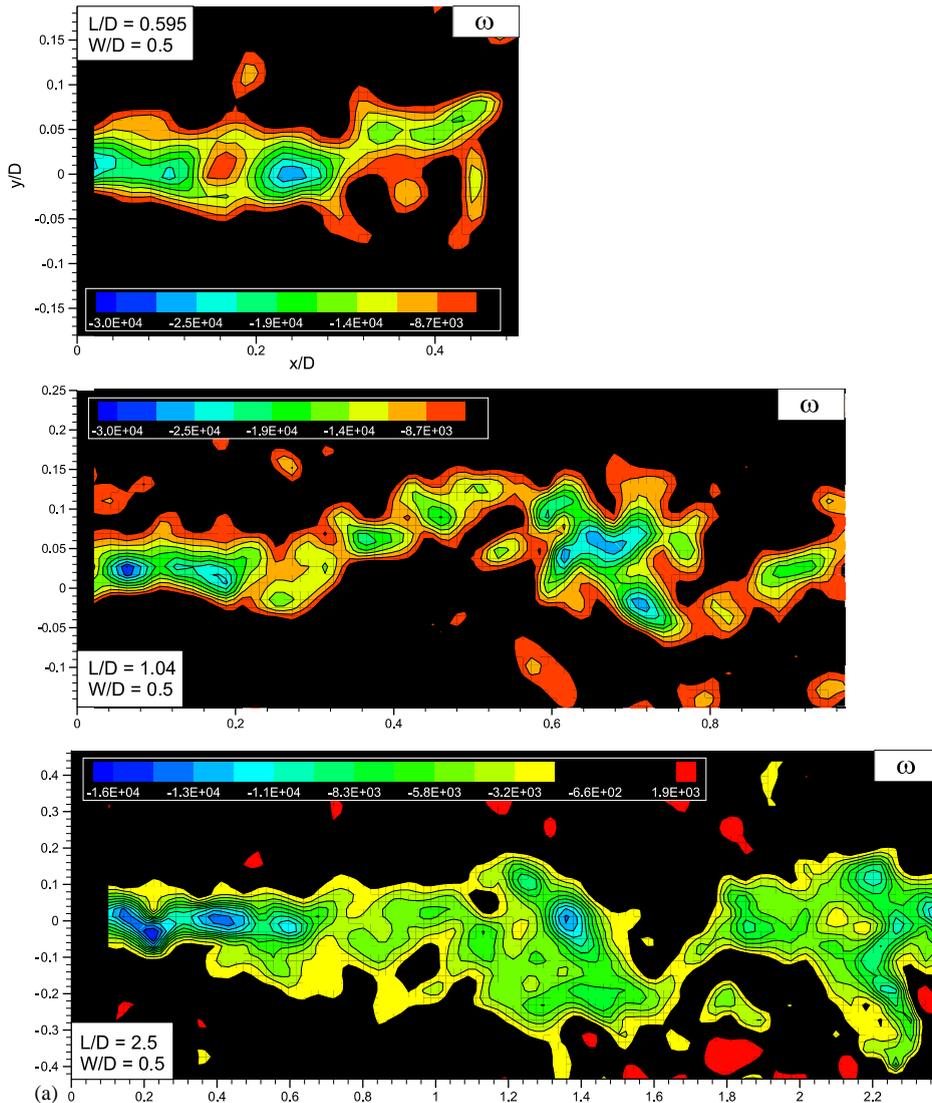
Fig. 5. (a) Comparison of patterns of instantaneous vorticity as a function of cavity length L at a constant value of cavity depth W, both of which are normalized by diameter D of the inflow pipe. For the top, middle, and bottom images, the minimum levels of vorticity $\omega_{min} = -8700$, -8700, and $-1900\,\mathrm{s}^{-1}$ and the incremental values are 2650, 2650, and $1300\,\mathrm{s}^{-1}$. These images (top to bottom) correspond to cases A, B and C in Fig. 3a. (b) Comparison of patterns of instantaneous velocity vectors $\mathbf{V}$ as a function of cavity length L at a constant value of cavity depth W, both of which are normalized by diameter D of the inflow pipe. These images (top to bottom) correspond to cases A, B and C in Fig. 3a. (c) Comparison of patterns of instantaneous transverse velocity v as a function of cavity length L at a constant value of cavity depth W, both of which are normalized by diameter D of the inflow pipe. For the top, middle, and bottom images, the minimum negative and positive levels of velocity are $v_{min}^- = -0.9$, -3.1, $-2.9\,\mathrm{m/s}$ and $v_{min}^+ = 4.2$, 4.8, $1.3\,\mathrm{m/s}$ and the incremental values are $\Delta v = 1.1$, 1.6, and $1.4\,\mathrm{m/s}$. These images (top to bottom) correspond to cases A, B and C in Fig. 3a.
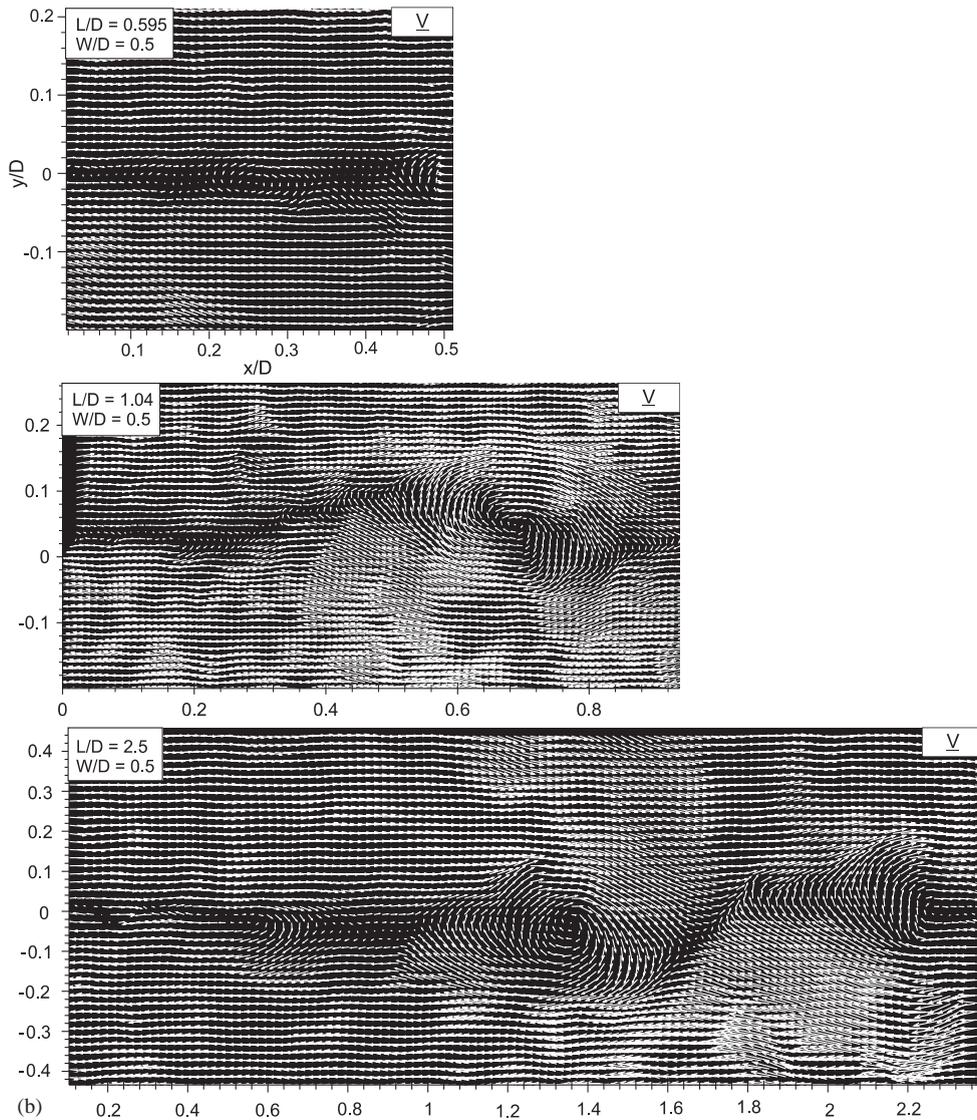
Fig. 5. (*Continued*)

A persistent characteristic in all of the images of Fig. 5a is the existence of small-scale concentrations of vorticity, which arise from an instability associated with the very high vorticity that occurs at the leading-corner of the cavity. They occur at a relatively high frequency, relative to the frequency of the flow tone, are not phase locked and, therefore, do not play a direct role in the occurrence of the flow tone. It is expected, however, that the small-scale vortical structures will influence the values of Reynolds stress and instantaneous acoustic power generation in the initial region of the shear layer.

In summary, the principal elements of the locked-on patterns of instantaneous vorticity in Fig. 5a are: (a) substantial transverse deflections of the vorticity layer in cases where large-scale vortex formation does not occur; (b) formation of large-scale vortical structures. It appears that for short and moderate length cavities $L/D = 0.595$ and 1.04, mechanism (a) is clearly evident and, in fact, for the shortest cavity $L/D = 0.595$, it is the only mechanism. For sufficiently long cavity lengths, mechanism (b) is present, and, for the longest cavity $L/D = 2.5$, it appears to be the only and predominant unsteady feature of the shear layer.
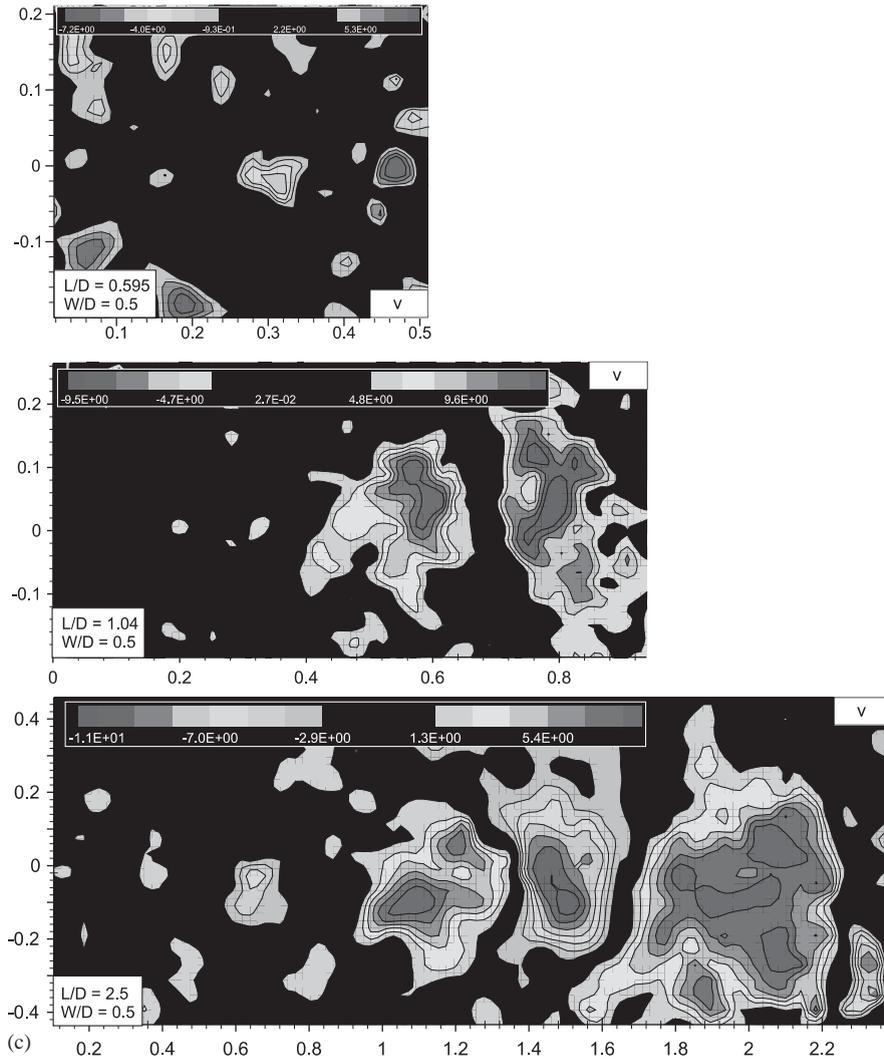
Fig. 5. (*Continued*)

4.2.2. Patterns of instantaneous total velocity

Fig. 5b shows patterns of instantaneous velocity vectors **V** in a reference frame moving at one-half the inflow velocity U; **V** represents the total velocity $\mathbf{V} = u\mathbf{i} + v\mathbf{j}$. They correspond to the vorticity pattern of Fig. 5a. The transverse deflections of the vorticity layer are reflected in the patterns of **V**. Moreover, the locations of the large-scale vortical structures of Fig. 5a are reaffirmed by large-scale swirl patterns of vectors. In addition, a well-defined swirl pattern tends to form at a location well upstream of the first large-scale swirl pattern in the image of $L/D = 2.5$. This initially formed swirl pattern suggests that the corresponding cluster of vorticity of Fig. 5a represents the initial stage of formation of the next large-scale vortex.

4.2.3. Patterns of instantaneous transverse velocity

An indication of the undulation of the shear layer along the cavity is the transverse velocity v. Fig. 5c shows patterns of constant contours of component v, which correspond to Figs. 5a and b. Comparison of the pattern in the middle image of Fig. 5c, which corresponds to $L/D = 1.04$, with the corresponding pattern of instantaneous vorticity in Fig. 5a, indicates that the center of the large-scale cluster of vorticity corresponds to the interface between the

concentrations of the v component of opposite sign. This same comparison holds for the longest cavity length $L/D = 2.5$.

The contours of constant v that dominate each of the images in Fig. 5c are associated with the large-scale vortical structures of Figs. 5a and b. For the image corresponding to $L/D = 2.5$, it is possible to evaluate the wavelength between vortical structures based on the center-to-center spacing of contours of constant v of like sign. On the other hand, the region of the initial upward deflection of the vorticity layer, which is evident in the top and middle images of Fig. 5a corresponding to $L/D = 0.595$ and 1.04, is not represented by the contours of constant v in the corresponding images of Fig. 5c.

5. Effect of cavity depth on locked-on and intermittent flow patterns: time-averaged and instantaneous images

5.1. Overview of time-averaged patterns of flow structure

The effect of cavity depth W on the patterns of time-averaged streamlines is shown in Fig. 6. As indicated in Section 2.1, unless otherwise indicated, all data and images correspond to the case of the short inlet pipe. Fig. 6 includes cases of both short and long inlet pipes. The top row of figures represents the case of a relatively short cavity with a short inlet pipe. In image (i), the recirculation cell is clearly evident. Image (ii) corresponds to a shallower cavity $W/D = 0.25$. It shows the upper portion of the streamline pattern due to the recirculation cell, which is located near the bottom right corner of the cavity.

Images (iii)–(v) of Fig. 6 represent the case of a long cavity. The patterns of images (iii) and (iv) correspond to the case of a short inlet pipe, and image (v) to the case of a long inlet pipe. In image (iii), for $W/D = 0.5$, the center of the recirculation cell is located at the bottom right corner of the cavity. The pattern of the shallower cavity $W/D = 0.25$ of image (iv) is differentiated from the pattern of the deeper cavity $W/D = 0.5$ in two respects. First of all, the center of the recirculation cell has moved from a position near the corner of the cavity to a location midway along the length, i.e., to $x/D = 1.25$. Second, downstream of this location, the flow tends to attach to the bottom wall of the cavity, then is deflected upward in the region near the corner of the cavity. A generally similar pattern of streamlines occurs in image (v) of Fig. 6, which corresponds to the long inlet pipe, as opposed to the short inlet pipe of image (iv). A well-defined recirculation cell is not indicated in the field of view of image (v); apparently it is located closer to the floor of the cavity. The major shift in the form of the streamline patterns of images (iv) and (v) is expected to retard the onset of flow tones. In fact, the critical velocity V_{cr} for onset of the flow tone is nearly twice as high for the cavity configuration of image (iv), relative to that of image (iii). Furthermore, the onset velocity V_{cr} is very large, i.e., a tone cannot be excited over the entire range of flow velocity, for the configuration of image (v).

Viewing all of the patterns of images (i)–(v) together, a well-defined recirculation cell, in absence of reattachment to the floor of the cavity, exists for images (i)–(iii). In all cases, well-defined flow tones are generated. On the other hand, in Figs. 6(iv) and (v), for which detectable or barely discernible recirculation cells occur approximately midway along the cavity, with subsequent reattachment to the floor of the cavity, the onset velocity V_{cr} for generation of a flow tone is substantially increased, or even infinite.

5.2. Averaged and instantaneous patterns of locked-on flow structure

For the case of a relatively shallow cavity $W/D = 0.25$, persistent and well-defined flow tones can be generated corresponding to the conditions of image (ii) in Fig. 6. In this case, the shear layer is allowed to develop in a relatively free fashion along its entire length, because a recirculation cell exists near the downstream corner of the cavity, and reattachment does not occur at the cavity floor.

Fig. 7 shows phase-averaged patterns of velocity $\langle V \rangle$ and vorticity $\langle \omega \rangle$, along with the instantaneous patterns of vorticity ω, during various phases of the oscillation cycle. The band of the pressure signal for each image is designated by the bold solid line. All images from a large sequence that fell within this band were employed in the phase-averaging process. The phase-averaged images shown in the left column of Fig. 7 involved an average of instantaneous images, one of which is shown in the right column. Viewing the overall features of the layer of vorticity in both the phase-averaged and instantaneous images, it is evident that it undergoes undulations, without formation of a large-scale concentration of vorticity, in contrast to the bottom two images of Fig. 5a. Furthermore, pronounced, small-scale concentrations of vorticity occur along the undulating shear layer. Their origin is described in conjunction with Figs. 3a, and 5a. They arise from a very small-scale instability at the leading-corner of the cavity. Comparison of the patterns of small-scale concentrations in the phase-averaged $\langle \omega \rangle$ and instantaneous ω patterns of vorticity
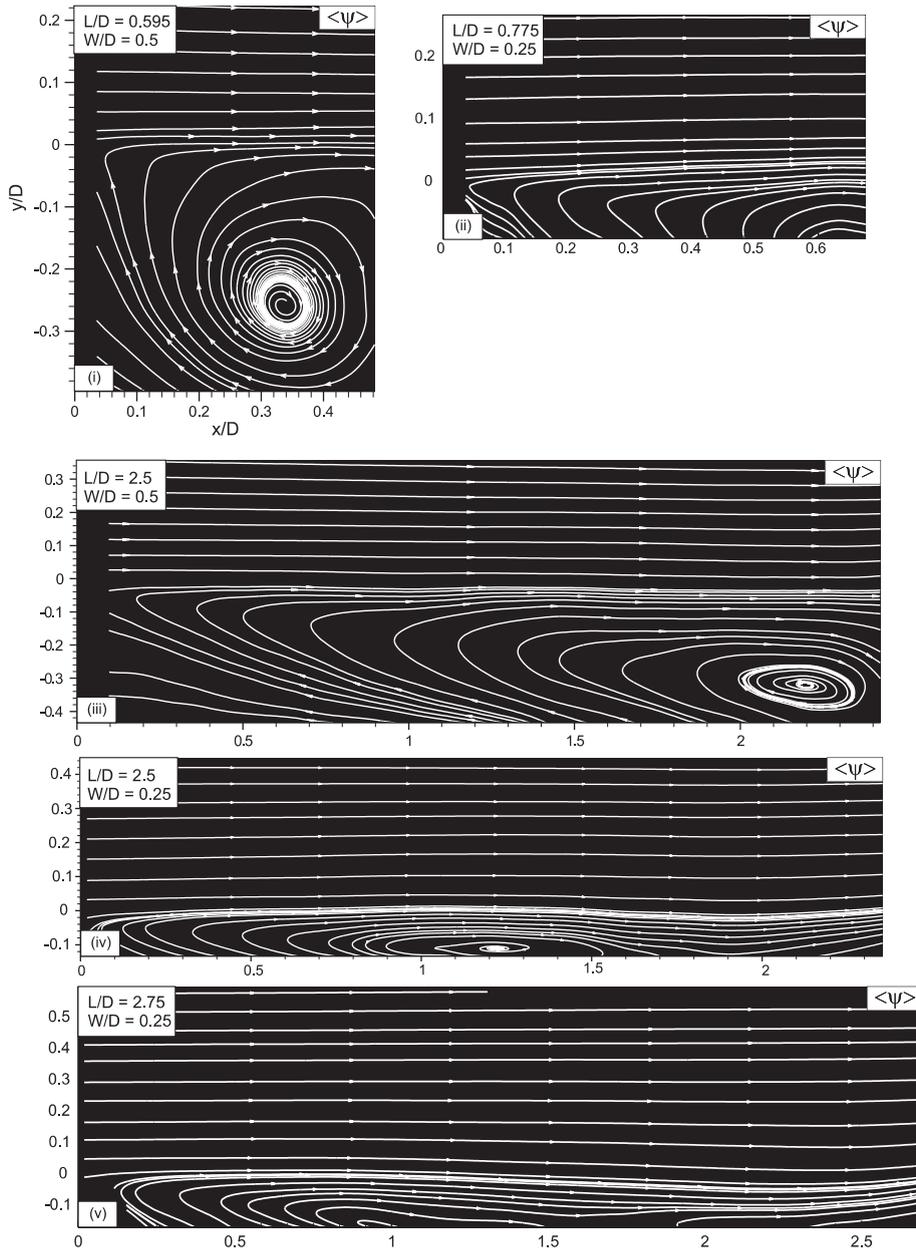
Fig. 6. Comparison of time-averaged streamline patterns showing effect of cavity depth *W* for relatively short and long cavities, represented by small and large values of cavity length *L*. Length *L* and depth *W* are normalized with respect to the inflow pipe diameter *D*. For all images, the inflow velocity is in the range of 35.97 to 39.62 m/s. Images at dimensionless depth $W/D = 0.5$ and $L/D = 0.595, 2.5$ correspond, respectively, to cases A and C in Fig. 3a. Images at dimensionless depth $W/D = 0.25$ and $L/D = 0.775, 2.5$ correspond, respectively, to cases D and E in Fig. 3b.

shows that they are not phase-locked with respect to the overall undulation of the shear layer. This lack of phase locking is due to the fact that the characteristic frequency of these very small-scale concentrations is much higher than the frequency corresponding to the long wavelength undulation of the vorticity layer, which corresponds to the small-scale mode defined by Rockwell et al. (2003). The frequency of this undulating layer corresponds to the frequency of the flow tone.
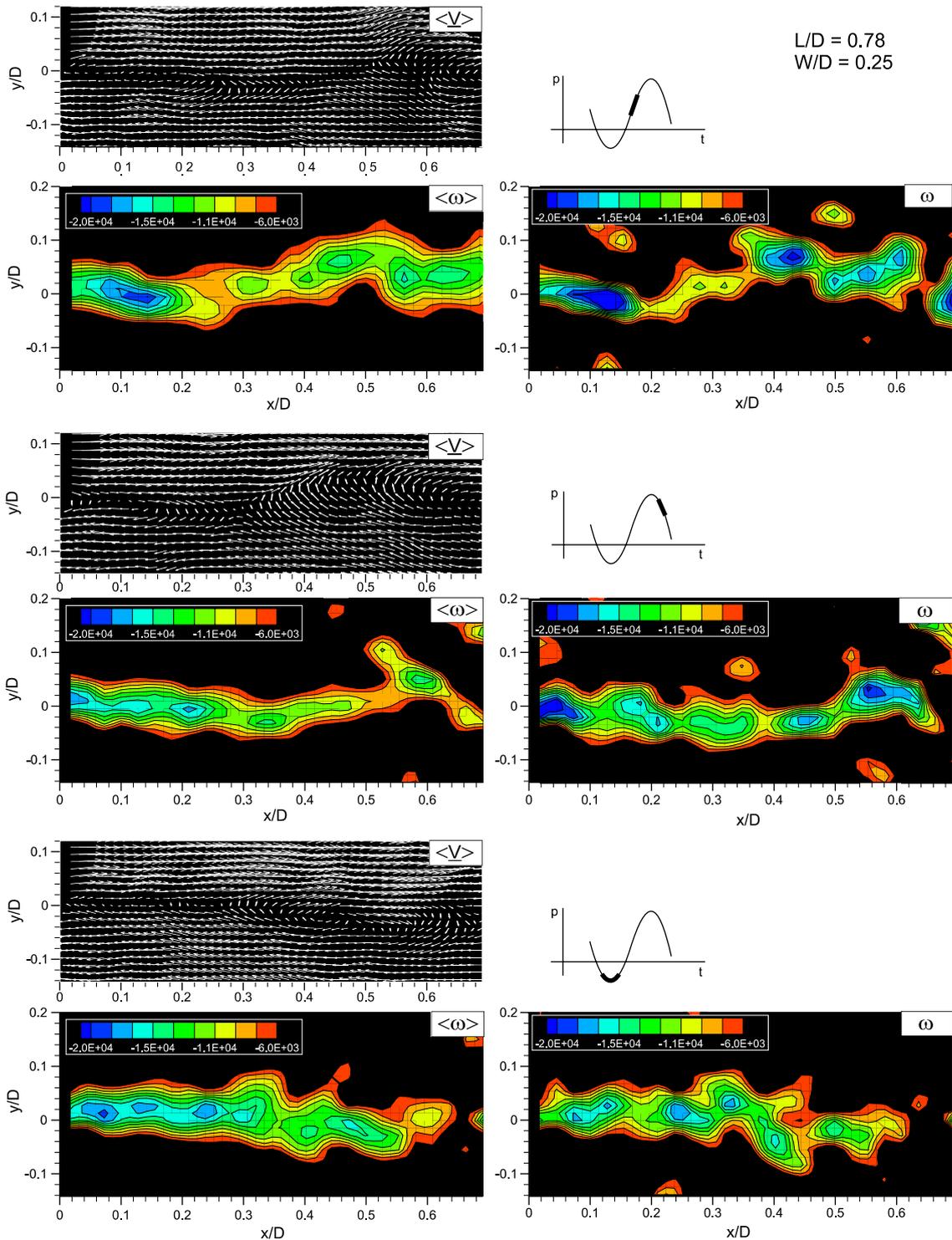
Fig. 7. Patterns of phase-averaged velocity $\langle \mathbf{V} \rangle$ and vorticity $\langle \omega \rangle$, along with corresponding instantaneous representations of vorticity ω for three different values of phase during the oscillation cycle. Dimensionless cavity length is $L/D = 0.778$ and cavity depth $W/D = 0.25$, in which D is the diameter of the inflow pipe. For all images, the minimum contour level is $\omega_{\min} = -6000\,\text{s}^{-1}$, and the incremental value is $\Delta\omega = 1333\,\text{s}^{-1}$. All images correspond to case D in Fig. 3b.

5.3. Averaged and instantaneous patterns of intermittent flow structure

Fig. 8a shows an overview of the time-averaged characteristics of a relatively shallow $W/D = 0.25$ cavity, which has a substantially longer length $L/D = 2.5$, in comparison with that of Fig. 7, for which $L/D = 0.78$. As already addressed in Fig. 6, the consequence is relocation of the center of the recirculation cell and occurrence of flow reattachment to the floor of the cavity; (see image (iv) in comparison with image (ii) of Fig. 6). The time-averaged patterns indicate a number of distinctive features, relative to a deeper cavity of the same length, which is shown in the bottom set of images of Figs. 4a–c. Flow reattachment to the floor of the cavity for the case of Fig. 8a, in contrast to no reattachment shown in Fig. 4a, along with the upward deflection of the flow near the trailing region of the cavity in Fig. 8a, yields the following features. The pattern of v_{rms} is actually partitioned into two distinct regions for the image of Fig. 8a; this boundary between the two regions occurs at $x/D = 1.65$, which is the approximate location at which the flow tends to reattach to the floor of the cavity, as indicated in the streamline pattern at the top of Fig. 8a. Such partitioning into two distinct regions of v_{rms} does not occur for the deeper cavity of Fig. 4b. The patterns of Reynolds stress correlation $\langle u'v' \rangle$ shown in Fig. 8a are deflected upward towards the trailing region of the cavity. Furthermore, the peak values of this Reynolds stress correlation $\langle u'v' \rangle$ in Fig. 8a are of the order of one-half the peak values associated with the deeper cavity of Fig. 4c.

The time-averaged images of Fig. 8a do not correspond to a classical, locked-on flow tone, unlike those of the aforementioned cases shown in Figs. 4a–c for deeper ($W/D = 0.5$) cavities of different length L/D. Examination of a large number of instantaneous images corresponding to the averaged images of Fig. 8a, shows that the flow structure was highly intermittent. For short durations of three to five cycles, however, the instantaneous pressure signal was nearly sinusoidal, indicating a short-term, highly organized behavior. Images corresponding to a given instant during the sinusoidal oscillation of the shear layer are given in Fig. 8b. They are compared directly with locked-on images for the deeper cavity $W/D = 0.5$ of the same length $L/D = 2.5$. These instantaneous images were selected on the basis of appearance of the first, large-scale concentration of vorticity at a location approximately midway along the cavity. All three types of representations, namely instantaneous vorticity ω, total velocity $\mathbf{V}$ and transverse velocity v clearly show the existence of large-scale vortical structures for both values of cavity depth W/D.

Considering, first of all, the patterns of instantaneous vorticity shown in the top set of images of Fig. 8b, the remarkable feature of the pattern for the shallower cavity $W/D = 0.25$ is the penetration of large-scale clusters of vorticity well above the mouth of the cavity, indicated by the elevation $y/D = 0$. Furthermore, in the downstream region of the cavity, in particular in the vicinity of the trailing (impingement) corner, the occurrence of a coherent cluster of vorticity is not apparent, in contrast to the case of the deeper cavity $W/D = 0.5$. These general features are reflected in the patterns of instantaneous velocity shown in the middle set of images. In general, large-scale swirls of $\mathbf{V}$ are centered at locations where well-defined, large-scale vorticity clusters occur in the top set of images.

A further indicator of the large-scale structures is the image of contours of constant transverse velocity component v. Contours of constant positive and negative v at the bottom of Fig. 8b are located immediately adjacent to each other and are approximately centered on the large-scale vorticity cluster, at least for the upstream large-scale vortex for the case $W/D = 0.5$. For the case of the shallow cavity $W/D = 0.25$, the large-scale cluster of vorticity and sets of contours of positive and negative v are not as evident, presumably due to displacement of the recirculation cell to the middle of the cavity and the tendency toward reattachment in the downstream region of the cavity, both of which would promote distorted patterns of v relative to the deeper cavity.

6. Effect of cavity geometry on locked-on and intermittent flow patterns: overview of classes of response

In the foregoing sections, various locked-on and intermittent states of the shear layer past the cavity have been defined in terms of time-averaged and instantaneous flow patterns. Fig. 9 provides an overview of locked-on and intermittent states, with a direct comparison of time traces and spectra. The states represented by the sets of images of Fig. 9 are as follows: locked-on flow tone; locked-on flow tone with modulation; and non-locked-on tone generation with short-term oscillating states. In the following, each of these states is described in further detail.

6.1. Locked-on flow tone

Images (i) and (ii) of Fig. 9 correspond to the case of transverse undulations of the shear layer with embedded small-scale vortical structures. Large-scale vortex formation does not occur. For both images, the shear layer is deflected in the upward direction at the instant of image acquisition. For these images, as well as all others acquired during the long
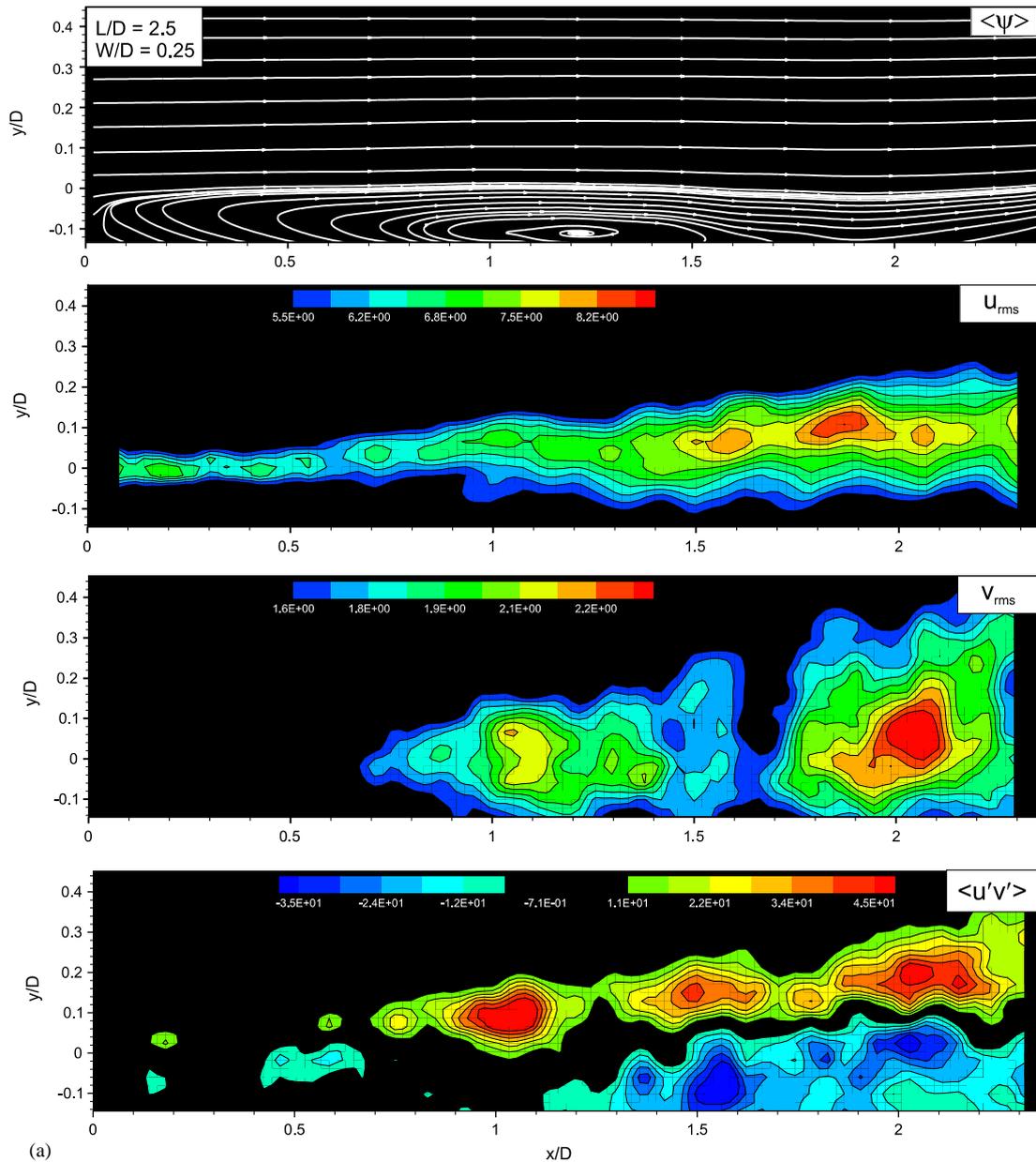
Fig. 8. (a) Time-averaged representations of the unsteady shear layer along the cavity for a relatively long cavity of length $L/D = 2.5$ and shallow depth $W/D = 0.25$. The minimum values of the contours in each of the images are: $(u_{rms})_{min} = 5.5$ m/s; $(v_{rms})_{min} = 1.6$ m/s; $(\langle u'v' \rangle)_{min}^- = -9.6$ m^2/s^2; and $(\langle u'v' \rangle)_{min}^+ = 11$ m^2/s^2. Corresponding incremental values of contours are $\Delta u_{rms} = 0.35$ m/s, $\Delta v_{rms} = 0.1$ m/s, and $\Delta \langle u'v' \rangle = 6$ m^2/s^2. All images correspond to case E in Fig. 3b. (b) Direct comparison of instantaneous flow structure along a relatively long cavity $L/D = 2.5$ for moderate depth $W/D = 0.5$ and shallow depth $W/D = 0.25$. For the former case, the flow structure is predominantly locked-on, while for the latter, it exhibits substantial intermittency, and the selected images correspond to a locally sinusoidal oscillation. For the contours of constant vorticity ω, the minimum levels are $\omega_{min} = -500$ and -2400 s^{-1} for the top and bottom images respectively. The corresponding incremental values are $\Delta \omega = 300$ and 1700 s^{-1}. For the bottom set of images, the minimum negative and positive contour levels are $(v)_{min}^- = -1.8$ m/s, $(v)_{min}^+ = 3.1$ m/s, and $(v)_{min}^- = -1.3$ m/s, $(v)_{min}^+ = 2.3$ m/s for the upper and lower images respectively, and the corresponding incremental values are $\Delta v = 1.7$ and 1.9 m/s respectively. Images for $W/D = 0.5$ and 0.25 correspond, respectively, to cases C and E in Figs. 3a and b.
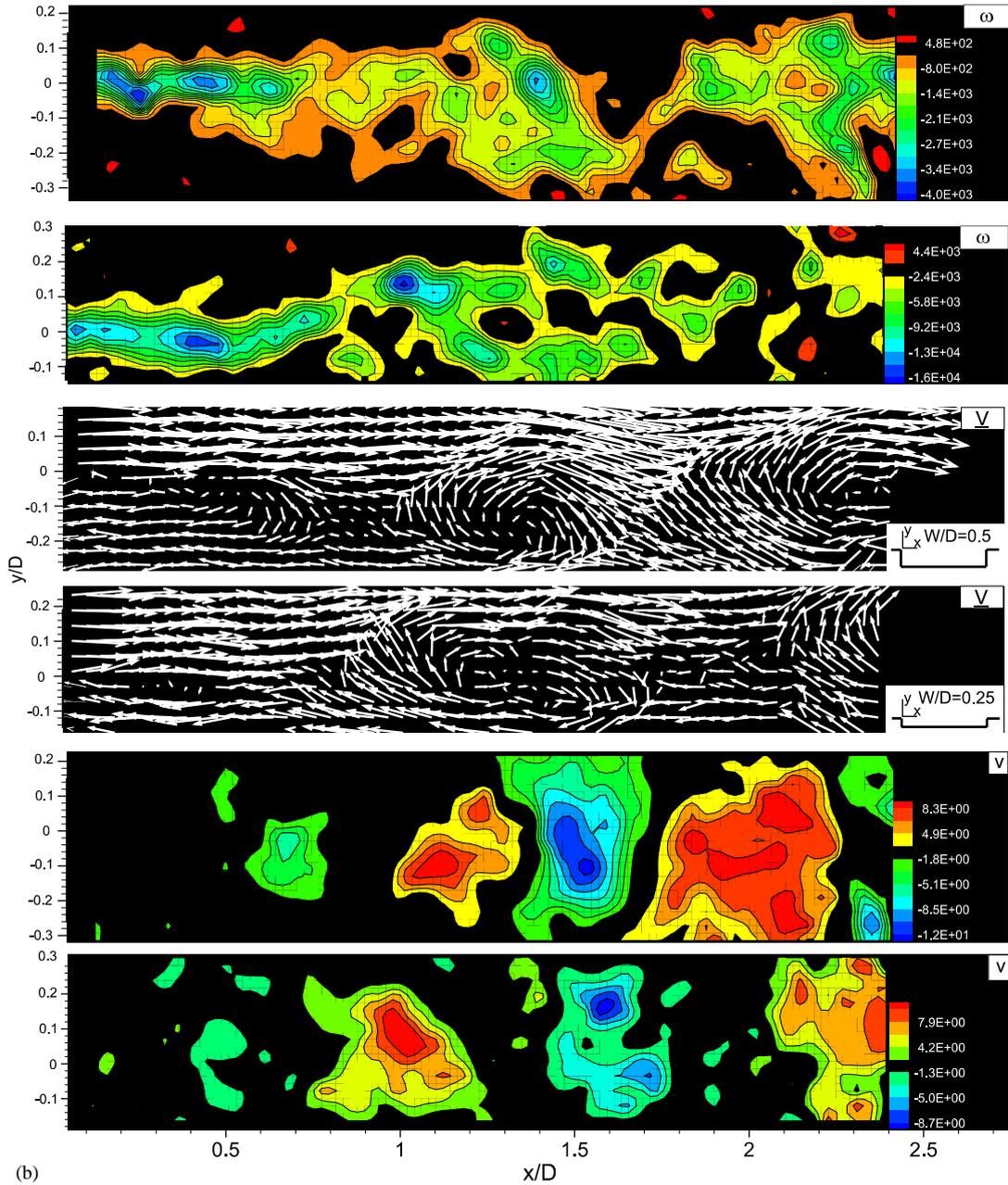
Fig. 8. (*Continued*)

sequence, the reference pressure signal showed relatively little amplitude modulation, as indicated in the inset. The corresponding spectrum for approximately 250 cycles of oscillation is shown immediately beneath this time trace. Furthermore, an expanded version of the spectral peak is shown at the right of images (i) and (ii). The Q-factor in this case is $Q = 2761$, indicating a sharply defined flow tone.

6.2. Locked-on flow tone with modulation

For the middle set of images (iii) and (iv), the predominant locked-on state of the flow structure, is represented by image (iii). During occasional dropout, nonphase-locked images of the type (iv) were observed in the large set of
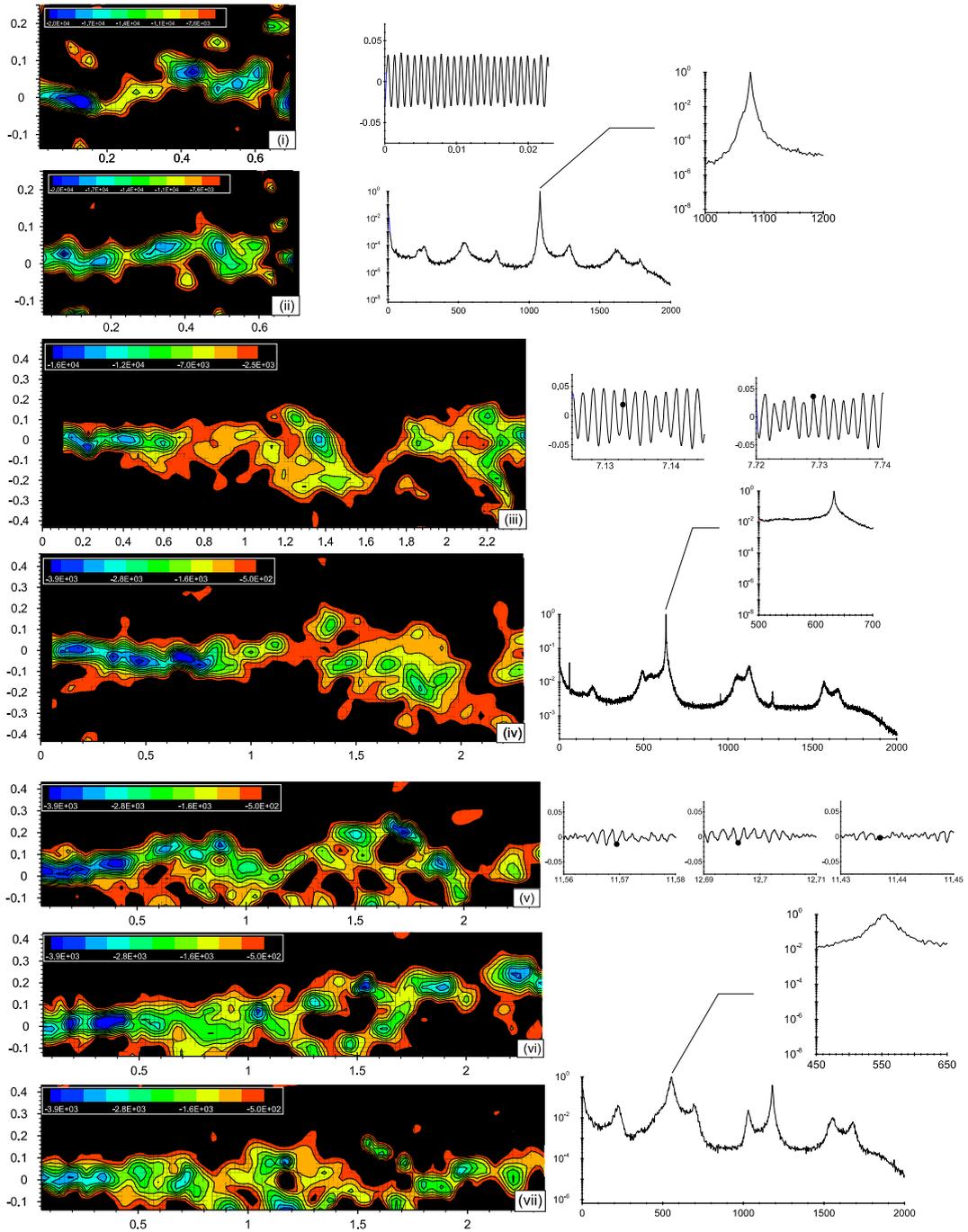
Fig. 9. Comparison of images of instantaneous patterns of vorticity with time traces of the pressure fluctuation, along with time-averaged spectra and zoomed-in views of the predominant spectral peak for locked-on flow tone (top set of images); locked-on flow tone with modulation; and nonlocked-on flow tone with locally periodic states (bottom set of images). For the top, middle and bottom sets of images, the values of cavity length L/D and depth W/D are respectively: $L/D = 0.595$ and $W/D = 0.5$; $L/D = 2.5$ and $W/D = 0.5$; $L/D = 2.5$ and $W/D = 0.25$. These sets of images correspond respectively to cases A, C and E in Figs. 3a and b.

acquired images. The representative time traces exhibits significant amplitude modulation, yet the predominant spectral peak is relatively sharp. The stretched version of this predominant peak is shown at the right of images (iii) and (iv). The Q-factor is $Q = 1180$, based on 250 cycles of oscillation. It clearly corresponds to a flow tone, but its value is approximately half of that corresponding to images (i) and (ii).

6.3. Non-locked-on tone generation WITH short-term coherent states

Images (v)–(vii) correspond to the highly intermittent states of the shear layer, as described in Section 5.3. In this case, the time traces in the vicinity of the instant of image acquisition are shown for each respective image. Images (v) and (vi) represent highly organized oscillations, whereas image (vii) is associated with a period of nonoscillatory behavior of the shear layer. The time-averaged spectrum obtained from an average of 250 cycles of oscillation, including the states represented by images (v)–(vii), yields the time-averaged spectrum as indicated, and the expanded version of the predominant spectral peak is also shown. The Q-factor for the time-averaged spectrum is $Q = 56$, which is substantially lower than for the sets of images shown at the top and middle of Fig. 9, despite the fact that locally periodic oscillations occur in the time trace.

7. Acoustic power generation due to shear layer along the cavity

7.1. Relation of flow patterns to acoustic power integral

According to Howe (1975, 1980), the instantaneous acoustic power $P_{ac}(t)$ generated by the flow in volume $\mathscr{V}$ can be calculated according to

$$P_{ac} = -\rho_0 \int_{\mathscr{V}} \mathbf{u}_{ac} \cdot (\boldsymbol{\omega} \times \mathbf{V}) \, d\mathscr{V}, \tag{7.1}$$

where ρ_0 is fluid density, $\mathbf{u}_{ac} = u_{acx}\mathbf{i} + u_{acy}\mathbf{j} + u_{acz}\mathbf{k}$ is acoustic (irrotational) velocity field, $\mathbf{V} = V_x\mathbf{i} + V_y\mathbf{j} + V_z\mathbf{k}$ is hydrodynamic (incompressible) velocity field, and $\boldsymbol{\omega}$ is the vorticity defined according to

$$\boldsymbol{\omega} = \boldsymbol{\nabla} \times \mathbf{V}. \tag{7.2}$$

The integrand of Eq. (7.1) can be decomposed into streamwise and transverse projections as follows:

$$\{[\boldsymbol{\omega} \times \mathbf{V}]_x\mathbf{i} + [\boldsymbol{\omega} \times \mathbf{V}]_y\mathbf{j}\} \cdot \{\mathbf{u}_{acx}\mathbf{i} + \mathbf{u}_{acy}\mathbf{j}\}. \tag{7.3}$$

The vectors $\boldsymbol{\omega} \times \mathbf{V}$ were calculated for the three values of cavity length that correspond to the cases presented in Fig. 5a. The vorticity $\boldsymbol{\omega}$ and velocity $\mathbf{V}$ are instantaneous values; they were not decomposed into time-averaged and fluctuating components. This decomposition is addressed in Section 7.2.

Fig. 10a shows representations of the hydrodynamic component to the acoustic power integral for the case of a relatively short cavity ($L/D = 0.595$), which corresponds to the top image of Fig. 5a. Contours of constant vorticity are shown in the top plot of Fig. 10a. The bottom three plots show the distribution of the vectors $\boldsymbol{\omega} \times \mathbf{V}$, and their streamwise and transverse projections$[\boldsymbol{\omega} \times \mathbf{V}]_x$ and $[\boldsymbol{\omega} \times \mathbf{V}]_y$. These plots show relatively large, downward-oriented vectors, which are distributed along the shear layer that is defined by the contours of constant vorticity. The large negative values of the transverse component $[\boldsymbol{\omega} \times \mathbf{V}]_y$ are primarily due to high values of $\boldsymbol{\omega}$. Large values of the streamwise projection $[\boldsymbol{\omega} \times \mathbf{V}]_x$, of both positive and negative sign, also occur in the shear layer region. However, these contours of $[\boldsymbol{\omega} \times \mathbf{V}]_x$ do not show a well-defined pattern due to the absence of large-scale structures in the shear layer.

Fig. 10(b) corresponds to an intermediate value of cavity length ($L/D = 1.04$). The contour plot of vorticity is shown at the middle of Fig. 5a and is reproduced at the top of Fig. 10b. The bottom three plots show the distributions of the $\boldsymbol{\omega} \times \mathbf{V}$ vectors and their x and y components. As in the previous case, large, downward-oriented vectors are distributed along the shear layer. The large negative values of $[\boldsymbol{\omega} \times \mathbf{V}]_y$ immediately downstream of the leading edge of the cavity are due to the high levels of distributed negative vorticity in this region. The highest values of $[\boldsymbol{\omega} \times \mathbf{V}]_y$ occur at the location of the large-scale cluster of vorticity shown in the top plot of Fig. 10b. The contour plot of the streamwise component $[\boldsymbol{\omega} \times \mathbf{V}]_x$ shows that the significant values of the x component occur along the shear layer. In contrast to the short cavity case, the absolute values of $[\boldsymbol{\omega} \times \mathbf{V}]_x$ increase with increasing streamwise distance. Significant values of $[\boldsymbol{\omega} \times \mathbf{V}]_x$ of opposite sign are especially evident for the large-scale vortex shown in the top plot of Fig. 10b.

A relatively large value of cavity length is represented by the plots of Fig. 10c. This case corresponds to the bottom plot of Fig. 5a ($L/D = 2.5$). Similar to the case of the intermediate cavity length ($L/D = 1.04$), the larger vectors of the
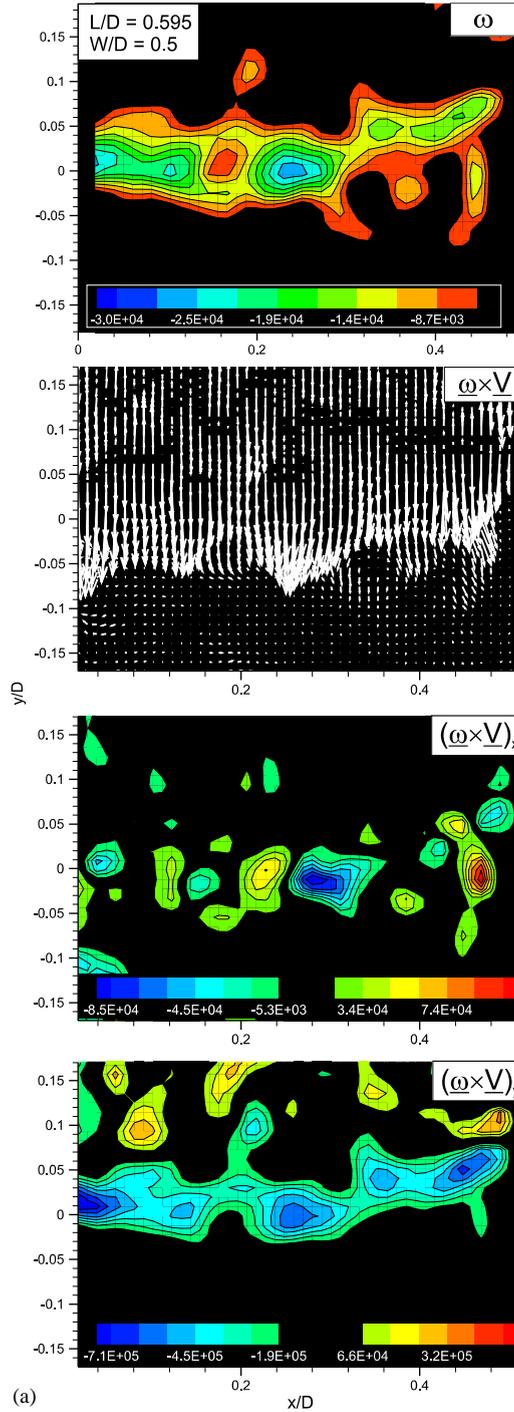
Fig. 10(a). Representations of the hydrodynamic contribution to the acoustic power integral for the case of a relatively short cavity represented by a relatively small value of L, normalized with respect to the diameter D of the inflow pipe. In the images, the minimum values of the contours are $(\omega)_{min} = -8700\,\mathrm{s}^{-1}$; $[(\boldsymbol{\omega} \times \mathbf{V})_x^-]_{min} = -5300\,\mathrm{m/s}^2$; $[(\boldsymbol{\omega} \times \mathbf{V})_x^+]_{min} = 20\,667\,\mathrm{m/s}^2$; $[(\boldsymbol{\omega} \times \mathbf{V})_y^-]_{min} = -190\,000\,\mathrm{m/s}^2$; and $[(\boldsymbol{\omega} \times \mathbf{V})_y^+]_{min} = 66\,000\,\mathrm{m/s}^2$; the corresponding incremental values are $\Delta\omega = 2650\,\mathrm{s}^{-1}$, $\Delta(\boldsymbol{\omega} \times \mathbf{V})_x = 13\,333\,\mathrm{m/s}^2$, and $\Delta(\boldsymbol{\omega} \times \mathbf{V})_y = 84\,667\,\mathrm{m/s}^2$. Images correspond to case A in Fig. 3a.

(b)
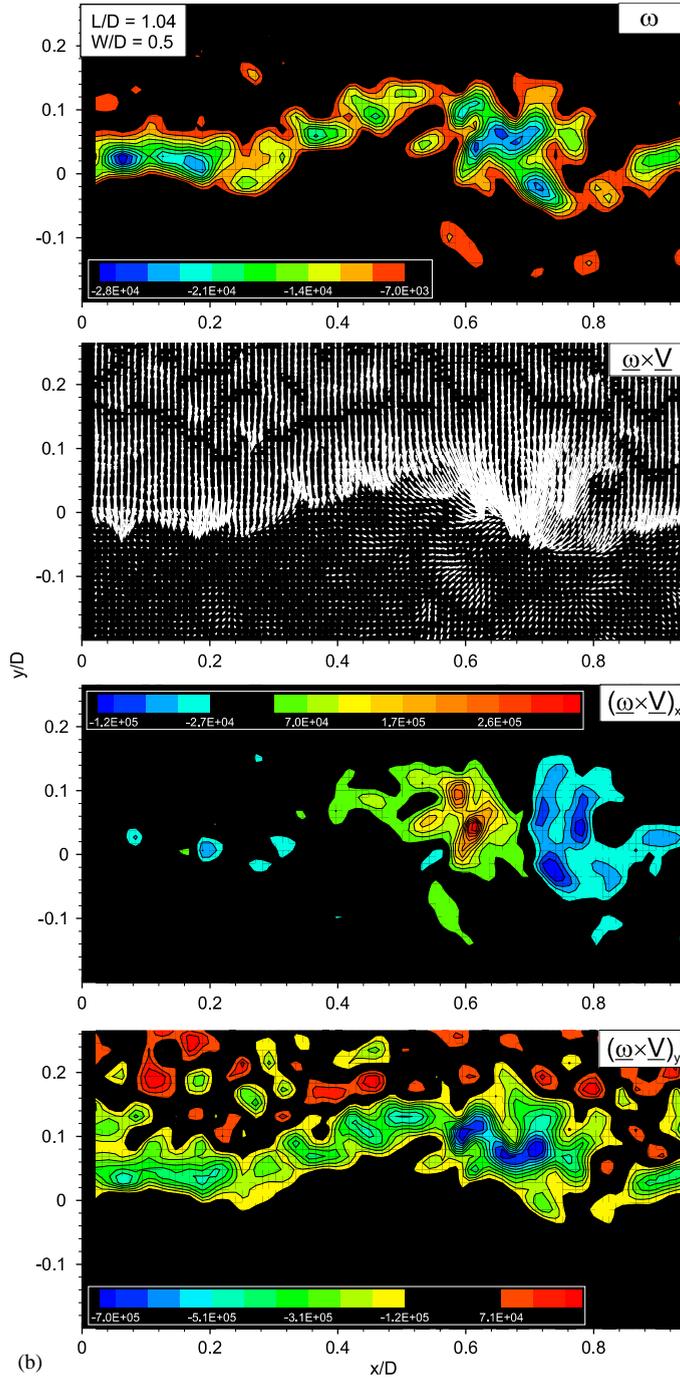
Fig. 10(b). Representations of the hydrodynamic contribution to the acoustic power integral for the case of an intermediate value of the cavity length L, normalized with respect to the diameter D of the inflow pipe. In the images, the minimum values of the contours are $(\omega)_{min} = -7000\,\mathrm{s^{-1}}$; $[(\omega \times \mathbf{V})_x^-]_{min} = -27\,000\,\mathrm{m/s^2}$; $[(\omega \times \mathbf{V})_x^+]_{min} = 36\,667\,\mathrm{m/s^2}$; $[(\omega \times \mathbf{V})_y^-]_{min} = -120\,000\,\mathrm{m/s^2}$; and $[(\omega \times \mathbf{V})_y^+]_{min} = 71\,000\,\mathrm{m/s^2}$; the corresponding incremental values are $\Delta\omega = 2333\,\mathrm{s^{-1}}$, $\Delta(\omega \times \mathbf{V})_x = 33\,333\,\mathrm{m/s^2}$, and $\Delta(\omega \times \mathbf{V})_y = 63\,333\,\mathrm{m/s^2}$. Images correspond to case B in Fig. 3a.
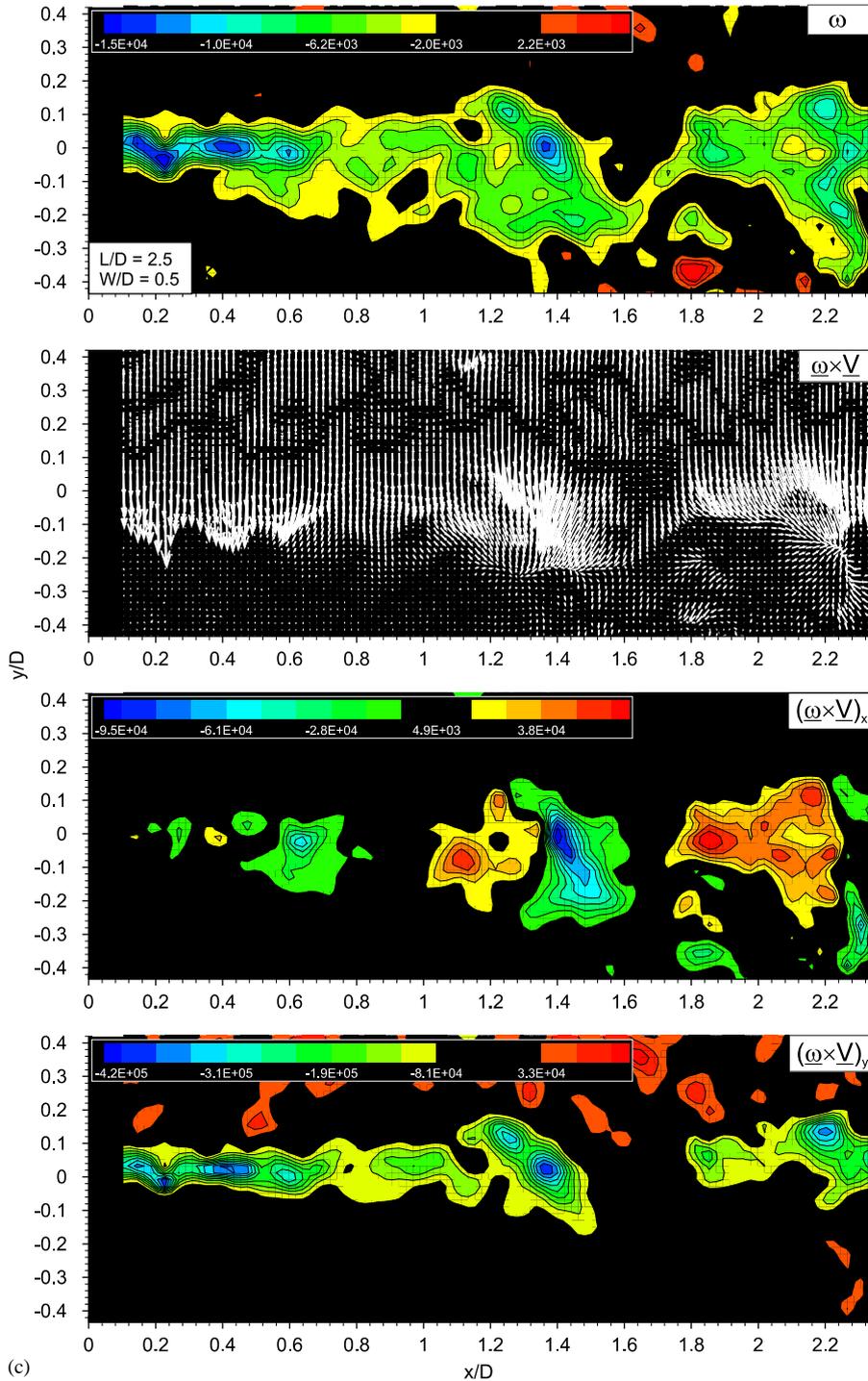
Fig. 10(c). Representations of the hydrodynamic contribution to the acoustic power integral for the case of a long cavity represented by a larger value of the cavity length L, normalized with respect to the diameter D of the inflow pipe. In the images, the minimum values of the contours are $(\omega)_{min} = -2000\,\text{s}^{-1}$; $[(\boldsymbol{\omega} \times \mathbf{V})_x^-]_{min} = -6100\,\text{m/s}^2$; $[(\boldsymbol{\omega} \times \mathbf{V})_x^+]_{min} = 15\,900\,\text{m/s}^2$; $[(\boldsymbol{\omega} \times \mathbf{V})_y^-]_{min} = -81\,000\,\text{m/s}^2$; and $[(\boldsymbol{\omega} \times \mathbf{V})_y^+]_{min} = 33\,000\,\text{m/s}^2$; the corresponding incremental values are $\Delta\omega = 1400\,\text{s}^{-1}$, $\Delta(\boldsymbol{\omega} \times \mathbf{V})_x = 11\,000\,\text{m/s}^2$, and $\Delta(\boldsymbol{\omega} \times \mathbf{V})_y = 36\,333\,\text{m/s}^2$. Images correspond to case C in Fig. 3a.

hydrodynamic contribution to the acoustic power $\boldsymbol{\omega} \times \mathbf{V}$ are distributed along the shear layer. The most significant values of the vertical component $[\boldsymbol{\omega} \times \mathbf{V}]_y$ occur immediately downstream of the leading corner of the cavity, due to the high values of vorticity distributed in this region, and in the regions corresponding to the two large-scale vorticity concentrations. In addition, the absolute values of $[\boldsymbol{\omega} \times \mathbf{V}]_x$ increase with increasing streamwise distance. The well-defined regions of the high values of $[\boldsymbol{\omega} \times \mathbf{V}]_x$ of opposite signs are due to the presence of the largest vortices.

The effectiveness of the acoustic power generation is determined by the dot product $(\boldsymbol{\omega} \times \mathbf{V}) \cdot \mathbf{u}_{ac}$. In turn, the values of the dot product depend on the relative direction of the hydrodynamic contribution vectors $\boldsymbol{\omega} \times \mathbf{V}$ and the acoustic particle velocity $\mathbf{u}_{ac}$. The direction of the acoustic particle velocity $\mathbf{u}_{ac}$ in the inlet and outlet pipes, as well as within the cavity away from its corners, is in the streamwise (x) direction. However, near the leading and trailing edges of the cavity, significant components in y direction are present. Therefore, a significant contribution to the acoustic power from the distributed vorticity is expected in the regions near the corners of the cavity. For the cases of long and intermediate cavity length, the large-scale vortices are also expected to contribute to the acoustic power integral due to the large value of the streamwise component $[\boldsymbol{\omega} \times \mathbf{V}]_x$ associated with them. It should be noted, however, that the concentrations of high values of $[\boldsymbol{\omega} \times \mathbf{V}]_x$ occur in pairs of opposite sign, which will tend to cancel their overall effect.

A central feature of all of the patterns of vectors $\boldsymbol{\omega} \times \mathbf{V}$ shown in Figs. 10a–c is the correspondence between regions of high mean vorticity and regions of large vector magnitudes $\boldsymbol{\omega} \times \mathbf{V}$. The role of mean vorticity in generation of acoustic power is described in detail in the next section.

7.2. Decomposition of acoustic power integral

In contrast to the usual approach of evaluating acoustic power generation via a succession of instantaneous states over an oscillation cycle in Howe's acoustic power integral (see Section 7.1), it is possible to represent the acoustic power in terms of time-averaged vorticity and velocity components, along with correlations between the acoustic particle velocity and the fluctuating components of vorticity and velocity.

In the case of a two-dimensional flow, ω_x, ω_y, u_{acz}, and V_z are equal to zero. Hence,

$$\boldsymbol{\omega} \times \mathbf{V} = (-\omega_z V_y)\mathbf{i} + (\omega_z V_x)\mathbf{j}. \tag{7.4}$$

Therefore, the integrand in Eq. (7.1) can be expressed as

$$(\boldsymbol{\omega} \times \mathbf{V}) \cdot \mathbf{u}_{ac} = (-\omega_z V_y)u_{acx} + (\omega_z V_x)u_{acy}. \tag{7.5}$$

To show the effects of steady and fluctuating components of the hydrodynamic velocity field on the acoustic power generation, a Reynolds decomposition can be applied to the corresponding variables of Eq. (7.5):

$$\mathbf{V} = \bar{\mathbf{V}} + \mathbf{V}' \quad \text{and} \quad \boldsymbol{\omega} = \bar{\boldsymbol{\omega}} + \boldsymbol{\omega}'. \tag{7.6}$$

Here, $\mathbf{V}'$ is the fluctuating component of the velocity vector, and $\bar{\mathbf{V}}$ is the mean component, which is defined as follows:

$$\bar{\mathbf{V}} = \lim_{T \to \infty} \left[\frac{1}{T} \int_0^T \mathbf{V}(t)\, \mathrm{d}t \right]. \tag{7.7}$$

The mean and fluctuating components of vorticity are defined in a similar fashion.

The first term on the right-hand side of Eq. (7.5) can be expressed as

$$(-\omega_z V_y)u_{acx} = -(\bar{\omega}_z + \omega_z')(\bar{V}_y + V_y')u_{acx} = -u_{acx}\bar{\omega}_z \bar{V}_y - u_{acx}\bar{\omega}_z V_y' - u_{acx}\omega_z' \bar{V}_y - u_{acx}\omega_z' V_y'. \tag{7.8}$$

Similarly, the second term on the right-hand side of Eq. (7.5) becomes

$$(\omega_z V_x)u_{acy} = (\bar{\omega}_z + \omega_z')(\bar{V}_x + V_x')u_{acy} = u_{acy}\bar{\omega}_z \bar{V}_x + u_{acy}\bar{\omega}_z V_x' + u_{acy}\omega_z' \bar{V}_x + u_{acy}\omega_z' V_x'. \tag{7.9}$$

To sustain the lock-on, the acoustic power generated during *one period of acoustic velocity fluctuation* must be positive. Moreover, it has to be sufficiently large to overcome the inherent damping of the system. To estimate the contribution of each of the terms considered above, the average of Eq. (7.8) over one period of acoustic velocity fluctuation can be obtained:

$$[(-\omega_z V_y)u_{acx}]_a = -[u_{acx}\bar{\omega}_z \bar{V}_y]_a - [u_{acx}\bar{\omega}_z V_y']_a - [u_{acx}\omega_z' \bar{V}_y]_a - [u_{acx}\omega_z' V_y']_a. \tag{7.10}$$

Here, the average over one acoustic period is defined as follows:

$$[\xi]_a = \frac{1}{T} \int_0^T \xi(t)\, \mathrm{d}t. \tag{7.11}$$

In Eq. (7.11), ξ represents the parameter being averaged, and T is the period of the acoustic cycle. Since the mean components of velocity and vorticity are not time-dependent, Eq. (7.10) can be written as

$$[(-\omega_z V_y)u_{\mathrm{ac}x}]_a = -[u_{\mathrm{ac}x}]_a \bar{\omega}_z \bar{V}_y - [u_{\mathrm{ac}x} V'_y]_a \bar{\omega}_z - [u_{\mathrm{ac}x}\omega'_z]_a \bar{V}_y - [u_{\mathrm{ac}x}\omega'_z V'_y]_a. \tag{7.12}$$

The first term on the right-hand side of Eq. (7.12) is equal to zero because $[u_{\mathrm{ac}x}]_a = 0$. Moreover, the last term on the right-hand side of Eq. (7.12) can be neglected because it contains a product of fluctuating vorticity and velocity, each of which has an order of 0.1 of its respective mean value. Hence, Eq. (7.12) reduces to

$$[(-\omega_z V_y)u_{\mathrm{ac}x}]_a = -[u_{\mathrm{ac}x} V'_y]_a \bar{\omega}_z - [u_{\mathrm{ac}x}\omega'_z]_a \bar{V}_y. \tag{7.13}$$

Similarly, the averaging over one cycle of acoustic oscillation can be applied to Eq. (7.9):

$$[(\omega_z V_x)u_{\mathrm{ac}y}]_a = [u_{\mathrm{ac}y}]_a \bar{\omega}_z \bar{V}_x + [u_{\mathrm{ac}y} V'_x]_a \bar{\omega}_z + [u_{\mathrm{ac}y}\omega'_z]_a \bar{V}_x + [u_{\mathrm{ac}y}\omega'_z V'_x]_a, \tag{7.14}$$

which can be reduced to

$$[(\omega_z V_x)u_{\mathrm{ac}y}]_a = [u_{\mathrm{ac}y} V'_x]_a \bar{\omega}_z + [u_{\mathrm{ac}y}\omega'_z]_a \bar{V}_x. \tag{7.15}$$

Combining Eqs. (7.13) and (7.15) according to Eq. (7.5) yields the following expression for the net acoustic power generated over one cycle of acoustic oscillation

$$\begin{aligned} [P_{\mathrm{ac}}(t)]_a &= -\rho_0 \int_{\mathscr{V}} [(\boldsymbol{\omega} \times \mathbf{V}) \cdot \mathbf{u}_{\mathrm{ac}}]_a \, \mathrm{d}\mathscr{V} \\ &= -\rho_0 \int_{\mathscr{V}} \{-[u_{\mathrm{ac}x} V'_y]_a \bar{\omega}_z - [u_{\mathrm{ac}x}\omega'_z]_a \bar{V}_y + [u_{\mathrm{ac}y} V'_x]_a \bar{\omega}_z + [u_{\mathrm{ac}y}\omega'_z]_a \bar{V}_x\} \, \mathrm{d}\mathscr{V}. \end{aligned} \tag{7.16}$$

This form of the acoustic power integral emphasizes the role of averaged vorticity $\bar{\omega}_z$ and velocity $\bar{V}_y$ and $\bar{V}_x$ in relation to the correlations between the acoustic particle velocities $u_{\mathrm{ac}x}$ and $u_{\mathrm{ac}y}$, and the fluctuating vorticity ω'_z and velocities V'_x and V'_y. Contrary to intuition, the effects of, for example, averaged vorticity do not cancel out during the averaging process unless the correlation between $u_{\mathrm{ac}x}$ and V'_y is zero. Similar reasoning holds for the remaining three terms in Eq. (7.16). This correlation may be interpreted as, for example, the product of the magnitudes of $u_{\mathrm{ac}x}$ and V'_y, multiplied by the cosine of the phase angle between them, provided that $u_{\mathrm{ac}x}$ and V'_y are harmonic.

8. Concluding remarks

The present study has aimed to provide quantitative, wholefield global representations of flow–acoustic coupling during generation of a flow tone using a technique of high-image-density particle image velocimetry, with emphasis on the effects of streamwise length scale of the cavity.

For the relatively shallow cavities of interest herein, provided the cavity is sufficiently deep, a large-scale recirculation cell exists, and as the cavity length is varied, the center of the cell maintains approximately the same relative position adjacent to the downstream face of the cavity. This type of time-averaged recirculation pattern is conducive to the onset of flow tones; it allows growth of the instability in the free shear layer along the mouth of the cavity. On the other hand, if the cavity is sufficiently shallow, then the center of the recirculation cell is displaced in the upstream direction, and the flow tends to reattach to the floor of the cavity. This configuration of the recirculation cell is not conducive to generation of highly coherent flow tones.

Instantaneous patterns of the flow structure, in relation to the streamwise length and cavity, allow quantitative definition of the hydrodynamic modes (stages) of the shear layer for the case of turbulent inflow conditions. Such hydrodynamic modes of the shear layer involve: (i) lateral deflections in absence of large-scale vortex formation; (ii) formation of a single vortex; and (iii) formation of two vortices over the streamwise extent of the cavity. Each of these hydrodynamic modes can generate a locked-on flow tone.

Acquisition of wholefield, instantaneous images allows evaluation of the instantaneous hydrodynamic component of Howe's acoustic power integral. Spatial distributions of this component are directly compared with spatial distributions of vorticity. Furthermore, a new interpretation of the acoustic power integral is derived using a Reynolds decomposition approach. It is demonstrated that the contributions of the mean vorticity and velocity components do

not cancel out over an oscillation cycle unless certain correlations between acoustic velocity and fluctuating hydrodynamic velocity and vorticity have zero values.

Finally, the concept of locked-on flow tone generation is critically assessed, and states of purely locked-on flow tones, locked-on flow tones with modulation, and non-locked-on oscillations with short-term, highly coherent fluctuations are described using a combination of wholefield quantitative images and time traces and spectra of fluctuating pressure. In the context of these interpretations, the degree of phase locking of the flow patterns is most effectively characterized using instantaneous images of vorticity and the degree to which they appear at the same spatial position from one cycle to the next.

References

Blake, W.K., 1986. Mechanics of Flow-Induced Sound and Vibration, vols. 1 and 2. Academic Press, NY.

Bruggeman, J.C., 1987. Flow-induced pulsations in pipe systems. Doctoral Dissertation, Technical University of Eindhoven.

Bruggeman, J.C., Hirschberg, A., van Dongen, M.E.H., Wijnands, A.P.J., Gorter, J., 1989. Flow induced pulsations in gas transport systems: analysis of the influence of closed side branches. ASME Journal of Fluids Engineering 111, 484–491.

Bruggeman, J.C., Hirschberg, A., van Dongen, M.E.H., Wijnands, A.P.J., Gorter, J., 1991. Self-sustained aero-acoustic pulsations in gas transport systems: experimental study of the influence of closed side branches. Journal of Sound and Vibration 150, 371–393.

Cremer, L., Ising, H., 1967. Die selbsterregten schwingungen von orgelpfeifen. Acustica 19, 143–153.

Demetz, F.C., Farabee, T.M., 1977. Laminar and turbulent shear flow-induced resonances. AIAA Paper 77-1293.

Elder, S.A., 1978. Self-excited depth-mode resonance for a wall-mounted cavity in turbulent flow. Journal of Acoustical Society of America 64, 877–890.

Elder, S.A., Farabee, T.M., Demetz, F.C., 1982. Mechanisms of flow-excited cavity tones at low Mach number. Journal of the Acoustical Society of America 72, 532–549.

Geveci, M., Oshkai, P., Rockwell, D., Lin, J.-C., Pollack, M., 2003. Imaging of the self-excited oscillations of flow past a cavity during generation of a flow tone. Journal of Fluids and Structures 18 (6), 665–694.

Hofmans, G.C.J., 1998. Vortex sound in confined flows. Doctoral Dissertation, Technical University of Eindhoven.

Hourigan, K., Welsh, M.C., Thompson, M.C., Stokes, A.N., 1990. Aerodynamic sources of acoustic resonance in a duct with baffles. Journal of Fluids and Structures 4, 345–370.

Howe, M.S., 1975. Contributions to the theory of aerodynamic sound, with application to excess jet noise and theory of the flute. Journal of Fluid Mechanics 71, 625–673.

Howe, M.S., 1980. The dissipation of sound at an edge. Journal of Sound and Vibration 70, 407–411.

Howe, M.S., 1998. Acoustics of fluid-structure interactions. Cambridge Monographs on Mechanics (ISBN-0-521-63320-6).

Huang, X.Y., Weaver, D.S., 1991. On the active control of shear layer oscillations across a cavity in the presence of pipeline acoustic resonance. Journal of Fluids and Structures 5, 207–219.

Kriesels, P.C., Peters, M.C.A.M., Hirschberg, A., Wijnands, A.P.J., Iafrati, A., Riccardi, G., Piva, R., Bruggeman, J.-C., 1995. High amplitude vortex-induced pulsations in a gas transport system. Journal of Sound and Vibration 184, 343–368.

Landreth, C.C., Adrian, R.J., 1989. Measurement and refinement of velocity data using high-image-density analysis in particle image velocimetry. In: Adrian, R., Asanuma, T., Durão, D., Durst, F., Whitelaw, J. (Eds.), Applications of Laser Anemometry to Fluid Mechanics. Springer, Berlin, NY, pp. 484–497.

Lin, J.-C., Rockwell, D., 2001a. Oscillations of a turbulent jet incident upon an edge. Journal of Fluids and Structures 15, 791–829.

Lin, J.-C., Rockwell, D., 2001b. Organized oscillations of an initially-turbulent flow past a cavity. AIAA Journal 39, 1139–1151.

Nelson, P.A., Halliwell, N.A., Doak, P.E., 1981. Fluid dynamics of a flow excited resonance. Part I: experiment. Journal of Sound and Vibration 78, 15–38.

Nelson, P.A., Halliwell, N., Doak, P.E., 1983. Fluid dynamics of a flow excited resonance. Part II: flow acoustic interaction. Journal of Sound and Vibration 91, 375–402.

Oshkai, P., Rockwell, D., Pollack, M., 2005. Shallow cavity flow tones: transformation from large- to small-scale modes. Journal of Sound and Vibration 280 (3–5), 777–813.

Pollack, M.L., 1980. Flow-induced tones in side-branch pipe resonators. Journal of the Acoustical Society of America 7, 1153–1156.

Radavich, P.M., Selamet, A., Novak, J.M., 1999. Acoustic source location in flow-excited quarter wave resonators. In: Internoise 99, Fort Lauderdale, FL, December 6–8, pp. 341–346.

Rockwell, D., 1983. Oscillations of impinging shear layers. Invited Lecture, 20th Aerospace Sciences Meeting of AIAA, January 1981, Orlando, FL; AIAA Paper 81-0047; also see AIAA Journal 21, 645–664.

Rockwell, D., Schachenmann, A., 1982a. Self-generation of organized waves in an impinging turbulent jet at low Mach number. Journal of Fluid Mechanics 117, 425–441.

Rockwell, D., Schachenmann, A., 1982b. The organized shear layer due to oscillations of a turbulent jet through an axisymmetric cavity. Journal of Sound and Vibration 85, 371–382.

Rockwell, D., Lin, J.-C., Oshkai, P., Reiss, M., Pollack, M., 2003. Shallow cavity flow tone experiments: onset of locked-on states. Journal of Fluid and Structures 17, 381–414.

Schachenmann, A., Rockwell, D., 1980. A quasi-standing-wave phenomenon due to oscillating internal flow. ASME Journal of Fluids Engineering 102, 70–77.

Stoubos, A.K., Benocci, C., Palli, E., Stoubos, G.K., Olivari, D., 1999. Aerodynamically-generated acoustic resonance in a pipe with annular flow restrictors. Journal of Fluids and Structures 13, 755–778.

Ziada, S., 1994. A flow visualization study of flow–acoustic coupling at the mouth of a resonant side-branch. Journal of Fluids and Structures 8, 391–416.

Ziada, S., Bühlmann, E.T., 1992. Self-excited resonances of two-side-branches in close proximity. Journal of Fluids and Structures 6, 583–601.

Ziada, S., Shine, S., 1999. Strouhal numbers of flow-excited acoustic resonance of closed side branches. Journal of Fluids and Structures 13, 127–142.

Zoccola, Jr. P.J., 2000. Experimental investigation of flow-induced cavity resonance. NSWCCD-TR-2000/010 (June), Carderock Division, Naval Surface Warfare Center, West Bethesda, Md 20817-5700.